Master's Thesis

MSc Environmental Engineering

The impact of aviation emissions on the particle number concentration and particle size distribution

Author:
Horim Kim

Supervisor:
Dr. Stephan Henne
Dr. Christoph Hüglin
Dr. Xiaole Zhang
Prof. Dr. Jing Wang

A thesis submitted in fulfillment of the requirements for the degree Master of Science in Environmental Engineering

in the

Chair of Air Quality and Particle Technology
Department of Civil, Environmental and Geomatic Engineering

Zürich, May 2, 2022

ETH Zürich

Empa
Materials Science and Technology

Eidgenössische Technische Hochschule Zürich
Swiss Federal Institute of Technology Zurich

Declaration of originality

The signed declaration of originality is a component of every semester paper, Bachelor's thesis, Master's thesis and any other degree paper undertaken during the course of studies, including the respective electronic versions.

Lecturers may also require a declaration of originality for other written papers compiled for their courses.

I hereby confirm that I am the sole author of the written work here enclosed and that I have compiled it in my own words. Parts excepted are corrections of form and content by the supervisor.

Title of work (in block letters):

The impact of aviation emissions on the particle number concentration and particle size distribution

Authored by (in block letters):

For papers written by groups the names of all authors are required.

Name(s):	**First name(s):**
Kim	Horim

With my signature I confirm that

- I have committed none of the forms of plagiarism described in the 'Citation etiquette' information sheet.
- I have documented all methods, data and processes truthfully.
- I have not manipulated any data.
- I have mentioned all persons who were significant facilitators of the work.

I am aware that the work may be screened electronically for plagiarism.

Place, date	**Signature(s)**
02.05.2022, Zurich	김호림

For papers written by groups the names of all authors are required. Their signatures collectively guarantee the entire content of the written paper.

Disclaimer

The following document contains the uncorrected version of a student master's thesis which forms part of the master's studies in environmental engineering. The views expressed in this document do not necessarily represent the position or the views of either the academic supervisors or the Swiss Federal Institute of Technology Zurich (ETH Zürich).

Acknowledgement

I want to thank my two supervisors, Dr. Stephan Henne and Dr. Christoph Hüglin, who have guided me since my Master's Project and continued supervising me in a research internship and this Master thesis. They always provided me with valuable comments on my scientific works and taught me how to communicate with other researchers scientifically. I would also like to thank Dr. Xiaole Zhang for sharing his time for the meetings and countless email discussions on the thesis work. His responses always helped me to resolve the problems quickly. Last but not least, I would like to say a special thank you to Professor Jing Wang for his considerable insights on the thesis work.

SWISS FEDERAL INSTITUTE OF TECHNOLOGY
ETH ZÜRICH

Abstract

Master of Science in Environmental Engineering

The impact of aviation emissions on the particle number concentration and particle size distribution

by Horim Kim

Aviation emissions are considered a critical source of ultra-fine particles in the vicinity of airports. Numerous monitoring studies explored the characteristics of aviation emissions. However, the interpretation of observations can be challenging, because aviation emissions can often not easily be distinguished from contributions from other sources. Developing an air quality model would be another approach to investigate the aviation emission, overcoming this drawback of observation. The present study investigates the impact of aviation emissions from Zurich airport on a nearby monitoring site by developing a particle number (PN) emission inventory and simulating aerosol dispersion and its dynamics by computational models. Observational data from a measurement site near Zurich airport was used for validating the model simulations for hourly PN concentrations and particle size distributions. According to the emission inventory, the total annual PN emissions from Zurich airport were $2.09 \cdot 10^{24}$ [particles/year] in 2019, which was four times higher than that in 2020, $4.78 \cdot 10^{23}$ [particles/year], when air traffic was lower due to restrictions in response to the COVID-19 pandemic. It was found that about 70 % of the emissions were from the taxiing periods of the aircraft. The model simulations demonstrated that the aviation emissions could increase the hourly PN concentrations at the considered measurement site by a factor 2-10 above the background concentrations. In addition, the applied aerosol dynamics model computed particle size distributions and determined that a large portion of the PN from the aviation emissions were particles with a diameter between 10 and 30 nm. However, the simulated hourly PN concentrations were only weakly correlated with the observations. This was because of approximated information used to compute the PN concentrations in the current model set-up. In particular, limitations were detected in estimating background concentrations and utilizing empirical PN emission factors to convert the mass of fuel burnt to the number of emitted particles. Moreover, the study argued that initial conditions on the dispersion and dynamics model required additional studies to enhance the model performance, i.e., the hourly spatial distribution of the PN emissions and the particle size distributions of the aviation emissions at Zurich airport. Nevertheless, the present modeling study well distinguished the attribution of the aviation emission to the PN concentration at the monitoring station.

Contents

Abbreviations

ADS-B	Automatic Dependent Surveillance-Broadcast
EEA	European Environmental Agency
GRAL	Graz Lagrangian dispersion Model
GRAMM	Graz Mesoscale wind fields Model
ICAO	International Civil Aviation Organization
LTO	Landing and Take-Off
MAFOR	Multicomponent Aerosol FORmation model
NABEL	Swiss National Air Pollution Monitoring Network
OSTLUFT	Air quality monitoring of the eastern Swiss cantons and the Principality of Liechtenstein
PM	Particulate Matter
PN	Particle Number
SMPS	Scanning Mobility Particle Sizer
SVM	Support Vector Machine
UFP	Ultra-Fine Particle

1 Introduction

Adverse health effects of airborne particulate matter (PM) have been widely reported by many studies [1; 2; 3]. Over the years, scientists speculated that the smaller particles can deeply penetrate into the human body system (i.e., blood stream) and potentially contain enhanced toxicity due to its higher surface area than larger particles [4]. Hence, the importance of understanding ultra-fine particles (UFPs), PM with the diameters below 100 nm, has been emphasized since several decades [5; 6; 7]. Due to their sub-micron size and high mobility, UFPs can cause acute and chronic diseases in the human circulatory and respiratory systems [8; 9]. UFPs are not substantial when measuring the mass concentration of PM, however, they largely account for total particle number (PN) concentration especially in urban areas [10] and during nucleation events.

Characterizing the sources of UFPs is significant to regulate their emissions, thus to reduce their impacts on public health. UFPs are primarily emitted from combustion processes of the vehicles, but they are also formed during nucleation events, converting from gas to particle in the ambient environment [11]. It is widely known that road-traffic emissions can be a dominant source of the UFPs in urban environments [6]. Combustion emissions from gasoline and diesel engines have attracted attention by many researchers and policy-makers. Nevertheless, emissions from aircraft engines have been given less attention in urban environments, although they may also critically contribute to UFPs burdens in these areas. Indeed, the impacts of aviation emissions on the environment are more extensive than the road traffic. Exhaust gases from the aircraft do not only influence the surrounding area at the ground level, but they also pollute the troposphere and lower stratosphere during the cruise [12; 13]. Since the emission during the cruise was more influential in terms of its expansive route on the globe, it was more highlighted than the emission in other flight phases in the past. However, with the cleaner urban atmospheric environments by the air pollution reduction in the last few years, the impact of aviation emissions near (or at) the airports was getting emphasized.

Previous studies have discovered that aircraft emissions at the airport significantly affect nearby regions. Several field measurements of PN concentrations were carried out in the vicinity of airports around the world. For example, at the Schiphol airport [14], Netherlands, and the Rome-Ciampino city airport [15], Italy, the PN concentration increased three fold at the monitoring site when the wind blew from the airport. The monitoring site in Netherlands was located 7 km away from the airport, and that in Italy located beside the airport, 380 m away from the airport centeroid. The particle sizes during the wind blown from the airport were dominated by UFPs with diameters of 10 - 20 nm. Other studies [16; 17] at the two airports in South California, United States, stated that the impact of air-traffic on the PN concentration was more substantial than

that of road-traffic emission in regions within 1 km from the airport. Moreover, a study at the Los Angeles international airport [18] elaborated that aviation emission increases two fold the indoor PN concentration by infiltrating into the residences. A monitoring study has also been implemented near Zurich airport since 2019 [19]. The monitoring station (Kloten FELD) was located 2 km away from the center of the taxiing area of the airport and measured PN concentrations and particle size distributions. Similar to the studies conducted at other airports, the observations in Zurich indicated that the PN concentrations could increase 2 to 4 fold at times when the wind blows from the airport, and the median diameter of the particles at these times was less than 20 nm [19].

Numerous studies explored the characteristics of aviation emissions through direct field observations. However, the observation analysis has a drawback that it might not specify the source attribution between aviation emissions and other possible sources. For example in the case of the observations in Zurich, a highly trafficked motorway exists 400 m away from the monitoring station in the same direction as the airport. Hence, there is the possibility that road-traffic emissions contributed significantly to the high PN concentrations observed during advection from the airport area. To resolve the drawback of the field observation studies, developing an air quality model would be another approach to explore the characteristics of aviation emissions. Several studies have already attempted to apply air quality models to simulate the impact of aircraft emissions on the surroundings of different airports. By simulating the plumes from the aircraft engines, the increase of PM 2.5 concentrations by aviation emission was identified [20; 21]. A chemical transport model was utilized to evaluate the impact of aircraft emissions on O_3 and PM 2.5 in the troposphere [22]. Moreover, an air quality modeling study was also carried out for the aviation emission from Zurich airport, and it validated the simulated annual mean PN concentration with observations [23].

In the present study, the impact of aviation emissions from Zurich airport was investigated by analyzing hourly resolution PN concentrations and particle size distributions as observed at Kloten FELD and as simulated by an air pollution dispersion model. Note that the observations were different from the data utilized in the previous investigation in Zurich airport [23]. For simulating the atmospheric dispersion of the particles, total annual PN emission and its spatial distribution at the surrounding areas of the airport were developed. The PN emission inventory was utilized as area sources of the particles in the atmospheric dispersion model using a coupled Eulerian and Lagrangian model system GRAMM/GRAL [24; 25]. Previously, the GRAMM/GRAL model was applied to simulate the NO_x concentration map of 2013-2014 in the city of Zurich, and the study has proved that the temporal variability of the pollutant was well-documented at various scales [26]. Here, the GRAMM/GRAL model was offline coupled with the Multicomponent Aerosol FORmation (MAFOR) model [27] to take into account the mechanisms of the aerosol

dynamics during transport from the source (airport) to the observation location.

2 Materials and Methods

2.1 Monitoring site

Measurements of UFPs have been conducted at an air-quality monitoring site near Zurich airport since 2019. The monitoring site (Kloten FELD: 47.27° N, 8.35° E, 440 m.a.s.l) is part of the air quality monitoring carried out by the cantons of Eastern Switzerland and the principality of Liechtenstein (OSTLUFT) and is situated around 1 km east of Zurich airport and 440 m east of the motorway A51 [19]. Therefore, the PN concentrations strongly depend on wind direction and air- and road-traffic activities. The location of the monitoring site was moved by 110 m to the northwest on 2020-02-20 (from Gerlisbergstrasse to Feld). The impact of this shift on the measurement is expected to be negligible. During the move, however, the scanning mobility particle sizer (SMPS) for quantifying the PN concentration and its size distribution was replaced from a TSI 3034 to a TSI 3938N89 [19]. The former SMPS was with a Long differential mobility analyzer (DMA) which measures particles with a diameter greater than or equal to 10 nm and smaller than 500 nm. However, the newer SMPS utilized Nano DMA, which allowed measuring the diameter from 2.5 nm to 150 nm [19]. PN concentrations and median particle diameters at FELD were measured as 30-minute mean values. The measurements on other air pollutants (i.e., NO, NO_2, SO_2, O_3) and meteorological variables (i.e., wind direction, wind velocity, temperature, relative humidity, and precipitation) were also available. Particle size distributions were also recorded every 30 minutes, containing diameter(D_P), $dN/dlogD_P$ (dN: particle number per bin), and dN for each distribution bin. The dN/dlogDp was corrected by the penetration rate of inlet and diffusion losses. Despite the correction, the previous monitoring study [19] reported that the correction could caused high uncertainties on the measurement, especially for the small particles. For instance, the particles with a diameter less than 10 nm were lost more than 60 % in total. Nevertheless, as mentioned above, the observation data from the FELD station were used for validating the modeling results in the hourly resolution. PN concentration and particle size distributions were compared with the simulation results.

2.2 Particle number emission inventory

The particle number emission inventory in the current study consisted of two parts: (1) hourly-resolution PN emissions in different phases of the aircraft movement, (2) high-resolution (approximately 5 m × 5 m) 3-D spatial distribution of annual PN emission. First, Automatic Dependent Surveillance-Broadcast (ADS-B) data obtained from the

OpenSky Network [28] were utilized to produce the spatial and temporal distribution of the aircraft's activities (Section 2.2.1). Second, annual amounts of the fuel burnt by the aircraft at Zurich airport ($M_{fuel,annual}$) were calculated by using air-traffic statistics from Zurich airport [29; 30] and the landing and take-off (LTO) emission calculator of the European Environmental Agency (EEA) [31] (Section 2.2.2). Third, the mass of fuel burnt was then converted to the annual PN emissions by the particle emission factors following the same approach as in the previous study for the airport of Zurich [23] (Section 2.2.3). Finally, the annual PN emissions were temporarily and spatially distributed based on the distributions obtained from ADS-B data in the first step. The basic scheme on developing the PN emission inventory were illustrated in Figure 1.

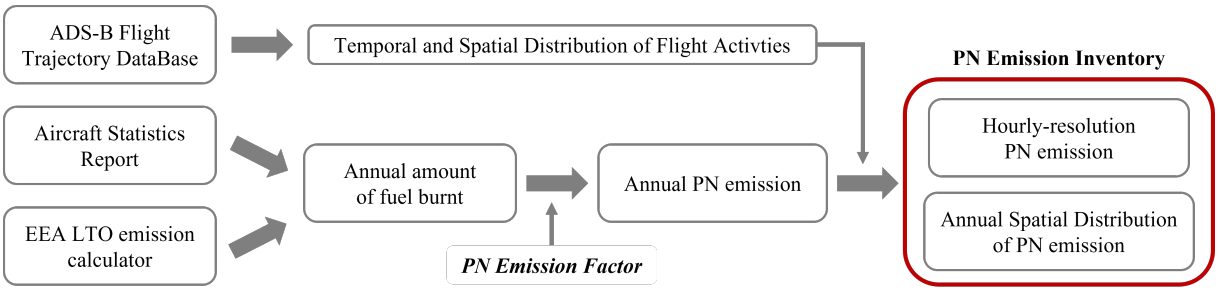

Figure 1: The flow scheme of developing the PN emission inventory from the reference information.

2.2.1 Flight trajectory database

ADS-B data from the OpenSky Network consists of non-profit, open-access air traffic control information that provides the individual flight trajectories [28] of most commercial and non-commercial flights to and from Zurich airport. The present study considered entire flight data in the year 2019 and 2020 at the surrounding areas of Zurich airport. The spatial domain was restricted by latitude (47.34° to 47.53° in WGS84 coordinate system) and longitude (8.48° to 8.64° in WGS84 coordinate system). In addition, the study only considered the flight trajectories with barometric altitude below 1,346 m. The air pollutant emission inventory guidebook from EEA [31] indicated that the flight movements above 3,000 ft (914 m) can be considered the cruise phase. This phase was neglected in the study because its impact on air quality at the ground level is very limited due to large vertical dilution of such emissions before reaching the ground [32]. Since the elevation of Zurich airport is 432 m above sea level [29], 1,346 m (914 + 432 m) was determined as the maximum altitude for the flight trajectories. The trajectory database contained the information of timestamp, latitude, longitude, International Civil Aviation Organization (ICAO) 24-bit code to identify flight type, speed, heading direction, on-ground sign, and barometric altitude. Based on the information, the trajectories were segmented into six phases: taxi, take-off, take-off roll, climb-out, approach, and landing roll, as shown in Figure 2.

After the segmentation, the total residence times of the aircraft (t_r) during the six phases (p) was calculated for each hour of the year (t_{id}, hour index of a year) to gain the temporal distribution of flight activities. The hourly duration of the residence time ($t_r(p, t_{id})$) was later used to distribute the $M_{fuel,annual}$ to hourly-resolution fuel burnt ($M_{fuel,hourly}$) (see Section 2.2.2). Moreover, the geographical information from the ADS-B data produced the annual spatial frequency maps of the flight activities for each phase, $t_{r,annual}(x, y, z, p)$. The spatial coordinates correspond to a 5 m × 5 m grid of the spatial domain (x,y) and continuous values of flight elevation from ADS-B data (z). The maps were further utilized to spatially distribute the annual PN emission.

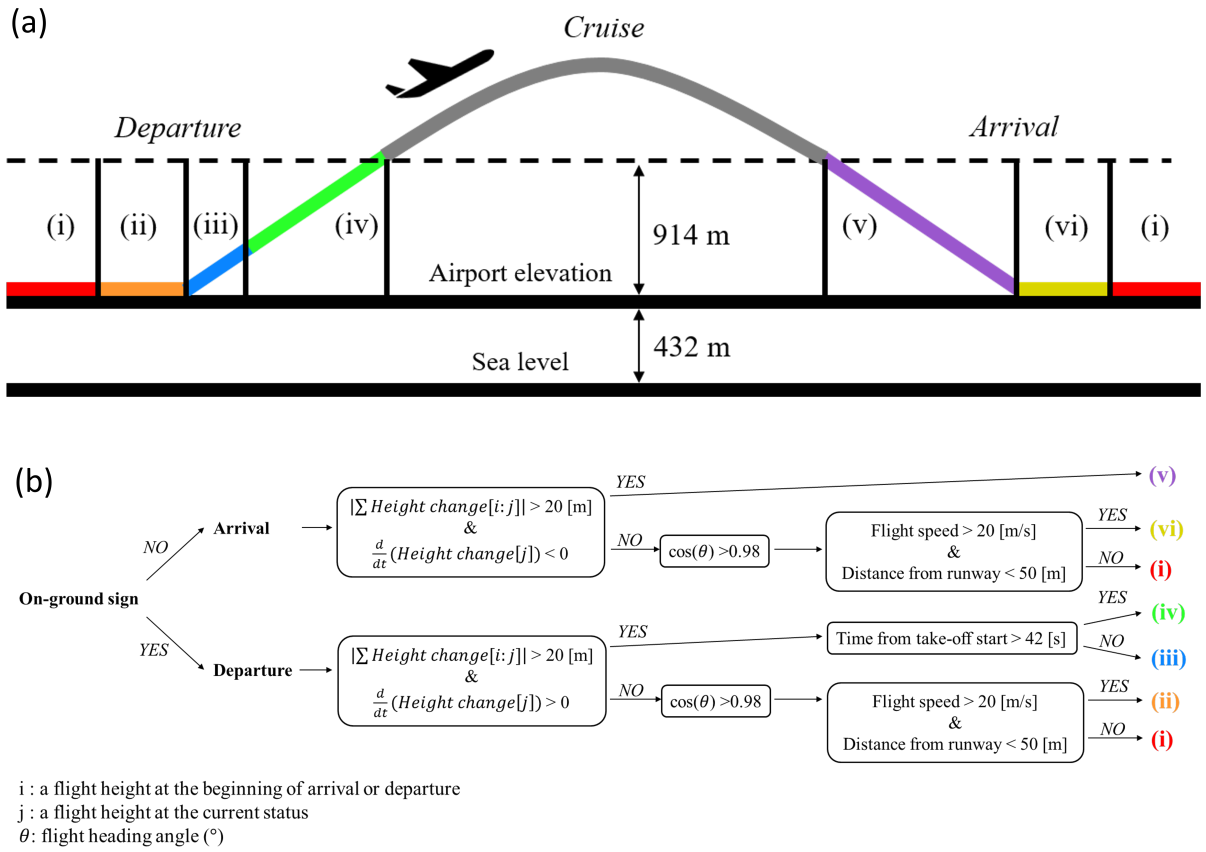

Figure 2: The segmentation of the aircraft fight trajectories: (i) taxi, (ii) take-off roll, (iii) take-off, (iv) climb-out, (v) approach, and (vi) landing roll. (a) illustrated periods of each flight phase on a flight trajectory from departure to arrival, and (b) elaborated detailed procedures on the segmentation.

2.2.2 Annual fuel consumption estimation

Zurich airport annually reports the traffic statistics of the number of aircraft movements and their types [29; 30] (see Appendix A1). In addition, the aviation LTO emission calculator from EEA [31] provides comprehensive mass-based emission estimates for different types of aircraft and engine models operated at European airports. It provides the mass of fuel burnt (M_{fuel}) and the mass of emitted gases (i.e., CO, HC, NOx) respectively

for five phases of flight movement: taxi-out, take-off, climb-out, approach and landing, and taxi-in. The calculator also considers an airport-specific time duration of each phase instead of taking the default phase duration values from the ICAO standard. For instance, the average taxi-in time and taxi-out time were taken from the LTO emission calculator as 316 and 782 seconds for Zurich airport in 2019, whereas the default values from the ICAO were 420 and 1140 seconds.

With the two datasets, the annual amounts of fuel burnt ($M_{fuel,annual}$) [kg] by aircraft at Zurich airport for the years 2019 and 2020 were obtained. The traffic statistics did not contain detailed information on the aircraft sub-types and the engine models. For example, the report informed that a total of 4,626 Airbus 340 arrived in 2019. However, it did not provide information on whether these flights were A340-300 with CFM56-5C4/P engines or A340-500 with Trent 553-61 engines. Therefore, among the multiple types of aircraft and engine models, the most common model of each aircraft type designated by the LTO calculator was taken into account in the calculation. Moreover, the LTO calculator only contains jet engine emission inventories but no data for turboprop and turboshaft engines. In such cases, the master emission calculator from the same EEA guidance [31] was used instead of the LTO calculator. At last, 11.7 % of aircraft types in 2019 and 25.4 % in 2020 were unlisted in the airport report (see Table 1). These unlisted flights consist of non-commercial flights (i.e., business flight, private flight, training flight) and other commercial flights (i.e., sightseeing flight, aerial work flight) [29; 30]. To comprehend these unlisted flights to the calculation, a scaling factor, f_{unid}, was multiplied to $M_{fuel,annual}$ from the listed aircraft (see Equation 1). Based on Equation 1, the $M_{fuel,annual}$ for five phases by each year were estimated as shown in Table 2. $N_{flight,i}$ is the number of flights for each aircraft type, and $M_{fuel}(i,p)$ is the mass of fuel burnt within each phase and aircraft type.

Table 1: Total number of flights per year counted by ADS-B database and Zurich airport statistics.

Year	ADS-B data	Traffic statistics		
		Listed flights	Unlisted flights	Total
2019	253,670	243,105	32,224	275,329
2020	111,511	83,076	28,252	111,328

$$M_{fuel,annual}(p) = \left(\sum_{i} N_{flight,i} \times M_{fuel}(i,p) \right) \times f_{unid} \tag{1}$$

$$\text{i} = \text{aircraft types},\ f_{unid} = \frac{\text{Number of total flights in the traffic statistics}}{\text{Number of listed flights in the traffic statistics}}$$

Table 2: The annual fuel consumption ($M_{fuel,annual}$) [kg] in 2019 and 2020 for the five flight phases calculated from the LTO calculator and Zurich airport statistics.

Year	Taxi-out	Take-off	Climb-out	Approach and Landing	Taxi-in
2019	56,617,505	29,578,325	76,250,537	47,493,716	22,873,423
2020	19,727,250	10,732,859	27,649,198	17,325,649	7,969,786

The five phases of the aircraft movement in the LTO calculator did not perfectly corresponded to the segmented phases of the ADS-B data. To adjust the estimated $M_{fuel,annual}(p)$ to the defined six phases (taxi, take-off, take-off roll, climb-out, approach, and landing roll), (i) the $M_{fuel,annual}$ in taxi-in and taxi-out are combined to a $M_{fuel,annual}$ in taxi period, (ii) the $M_{fuel,annual}$ in take-off is divided into the $M_{fuel,annual}$ for take-off/roll period and for actual take-off period respectively, and (iii) the $M_{fuel,annual}$ in approach and landing period is divided into the $M_{fuel,annual}$ for approach period and landing/roll period respectively. The partition of $M_{fuel,annual}$ from one phase to two different phases, in case of (ii) and (iii), was implemented based on the annual aircraft residence times in each phase (see Equation 2). As a result, the revised annual fuel consumption by the aircraft ($M^*_{fuel,annual}$) for the six phases were taken as given in Table 3.

$$M_{fuel,annual}(i) = \frac{\sum_{t_{id}=1}^{k} t_r(i, t_{id})}{\sum_{t_{id}=1}^{k} t_r(1, t_{id}) + \sum_{t_{id}=1}^{k} t_r(2, t_{id})} \tag{2}$$

$$\text{i = phase 1 or 2, k = hours per year}$$

Table 3: The revised annual fuel consumption ($M^*_{fuel,annual}$) [kg] in 2019 and 2020 for the six phases of the aircraft movements corresponding to segmented ADS-B data.

Year	Taxi	Take-off roll	Take-off	Climb-out	Approach	Landing
2019	79,490,929	13,516,481	16,061,844	76,250,537	21,511,222	25,982,494
2020	27,697,036	3,166,226	7,566,633	27,649,198	9,700,964	7,624,686

The $M^*_{fuel,annual}$ are then distributed to the hourly values, $M^*_{fuel,hourly}(p, t_{id})$, based on the temporal distribution of the flight activities from ADS-B data, $t_r(p, t_{id})$ (see Equation 3). The average fuel consumption per second for each phase $\overline{FF}(p)$ $[kg \cdot s^{-1}]$ was calculated by dividing $M^*_{fuel,annual}$ by the default duration of each phase from the LTO calculator (T_{def}) and the total number of the listed aircraft per year ($N_{flight,tot}$). The reason for deriving $\overline{FF}(p)$ is because the default duration of flight phases in the LTO emission calculator is different from the actual duration of flight activities from ADS-B data. Hence, $\overline{FF}(p)$ calibrated the effect of default assumption of phases' duration from

the LTO calculator. $M^*_{fuel,hourly}(p, t_{id})$ was obtained by multiplying $t_r(p, t_{id})$ [s] and $\overline{FF}(p)$ $[kg \cdot s^{-1}]$.

$$\overline{FF}(p) = \frac{M^*_{fuel,annual}(p)}{T_{def} \times N_{flight,tot}}$$
$$M^*_{fuel,hourly}(p, t_{id}) = \overline{FF}(p) \times t_r(p, t_{id}) \tag{3}$$

2.2.3 Particle number emission indices and estimation

Previous studies [33; 34; 35] demonstrated that ambient temperature, fuel sulfur composition, fuel aromatic content, and engine thrust level are significant factors influencing particle number emission from jet engines. In an earlier study by Zhang et al. (2020) [23], an empirical PN emission factor based on these four parameters (see Equation 4) was developed, making use of observational data from two aviation emission studies. One study measured the take-off engine emissions in the Los Angeles International (LAX) Airport [34], and the other study focused on the fuel compositions and engine emissions measured by NASA APEX (Aircraft Particle Emissions eXperiment), and AAFEX (Alternative Aviation Fuel EXperiment) I & II [33]. The former study was adapted to estimate the PN emission in 100 % thrust level, and the latter study was for 4 % and 7 % thrust level.

$$EI_N(S, T(t_{id}), F(p), A) = \frac{3.29 \times exp(-0.075 \times T(t_{id}) + 0.0017 \times F(p) + 0.017 \times A)}{1 + exp(-0.011 \times S + 2.54)} \tag{4}$$

$EI_N(\cdot)$ $[10^{16} \cdot kg^{-1} fuel]$ is the PN emission factor, S [ppm] is the fuel sulfur content by weight, T(t_{id}) [°C] is the ambient temperature in Zurich airport at each hour (t_{id}), F(p) [%] is the thrust level during the different flight phases, and A [%] is the fuel aromatic content by volume [23]. S and A were constant values selected as 650 ppm and 18 %, respectively, based on the average fuel composition measured during previous experimental studies at Zurich airport [36; 37]. For the thrust level, F(p), ICAO standard power settings were adopted for the taxi, take-off roll, take-off, and climb-out phases, as 7 %, 100 %, 100 %, and 85 %, respectively [23]. For the other phases, approach and landing/roll phase, both thrust levels were set as the same value in the taxi period (7 %) because a previous study at Copenhagen Airport [38] listed that the actual thrust levels during the final descent could be assumed as the idle engine power settings. Multiplying the PN emission factor with $M^*_{fuel,hourly}(p, t_{id})$, the hourly-resolution PN emission, $PN_{hourly}(p, t_{id})$, were obtained (see Equation 5).

$$PN_{hourly}(p, t_{id}) = EI_N(\cdot) \times M^*_{fuel,hourly}(p, t_{id}) \quad (5)$$

The spatial distribution of the annual PN emission, $PN_{annual}(x, y, z, p)$, was another important result from the PN emission estimation. The annual spatial distribution of the flight activities for each phase, $t_{r,annual}(x, y, z, p)$, were already acquired from the ADS-B data. Therefore, using $EI_N(\cdot)$, the average fuel consumption per second $\overline{FF}(p)$, and the $t_{r,annual}(x, y, z, p)$, the $PN_{annual}(x, y, z, p)$ was derived as Equation 6.

$$PN_{annual}(x, y, z, p) = EI_N(\cdot) \times \overline{FF}(p) \times t_{r,annual}(x, y, z, p) \quad (6)$$

2.3 Atmospheric dispersion model: GRAMM/GRAL

The atmospheric dispersion of the PN emission was simulated by the GRAMM/GRAL atmospheric dispersion system (Version 19.01) [24; 25]. The system comprises two models; the meso-scale wind field model GRAMM [39] and the Lagrangian dispersion model GRAL [40]. In the present study, GRAMM produced classified weather catalogues of the wind fields, stability class, the Obukhov length, and the friction velocity based on the observed meteorological data (e.g., wind speed, wind direction, stability class) taken from the MeteoSwiss station Zurich Kloten. Based on the GRAMM calculated wind field catalogue and the aviation emission inventory, GRAL calculated three-dimensional concentration fields.

The observed meteorological data for GRAMM in the current study were provided by the Kloten station near Zurich airport, which is a part of the MeteoSwiss SwissMetNet. Hourly wind speed and wind direction data from the station were directly utilized by the model. Stability classes were determined by a modified form of the solar radiation delta-T (SRDT) method given by the U.S. Environmental Protection Agency [41], which is recommended in the GRAMM/GRAL guideline [42]. The method estimates the Pasquill-Gifford stability categories, from A (most stable) to G (least stable), based on the status between daytime (solar radiation $> 20\ \mathrm{W}/m^2$) and nighttime (solar radiation $\leq 20\ \mathrm{W}/m^2$), wind speed, solar radiation, and the vertical gradient of the temperatures measured 2 m and 5 cm above the ground.

A grid system for the GRAMM domain (133 x 83 x 15 cells) was created with a horizontal resolution of 300 m and 15 vertical levels of layers up to 3,874 m (with the first layer at the height of 10 m above ground). In this study, an identical source of topography data as the previous study [23] was utilized, which was taken from the digital elevation data from the Shuttle Radar Topography Mission [43]. Moreover, the CORINE (Coordinate information on the environment) land cover data was provided by the Swiss

Federal Institute for Forest, Snow and Landscape Research (WSL) [44]. In general, the topography influenced the general wind flow pattern in GRAMM, and the land cover information determined the heat and water exchanges and surface roughness in the given area. However, building information was neglected in the model. It was hypothesized that the dispersion of aircraft emission in an open space of the airport was not significantly affected by the buildings.

GRAL calculated the atmospheric transport and dispersion of the PN emissions from Zurich airport to the surrounding areas using the wind field catalogue from GRAMM. Initially, the spatial distribution of the annual PN emission, $PN_{annual}(x, y, z, p)$, was imported from the emission inventory. The emission maps were considered in GRAL as area sources in the model domain. GRAL simulated the particle transport of the annual PN emission maps for different weather catalogues, and the results were converted to hourly series of the dispersion scenarios by matching each weather catalogue to the weather condition in each hour, and by distributing the annual concentration to hourly concentration with the hourly-resolution PN emission data, $PN_{hourly}(p, t_{id})$. For the general settings for GRAL, the dispersion time for each simulation was set to 3600 seconds, and the surface roughness was taken from the CORINE land cover data. Moreover, 358 Lagrangian particles per second were released during a simulation. To create a grid system of the GRAL domain, the horizontal resolution was set as 20 m, and the vertical dimension of the concentration layers was set as 3 m. As a result, the two-dimensional concentration fields (1983 x 1228 matrices) were obtained for each vertical layer. In this study, the layer of 2 m above the ground was explored and compared to observations. Note that GRAL calculated the concentration in a layer with the height defined by (the height above ground) $\pm$ 0.5 $\times$ (the vertical dimension) [42].

2.4 Aerosol dynamics model: MAFOR

The Multicomponent Aerosol FORmation (MAFOR) model was used to simulate the aging of emitted particles during the simulated atmospheric transport and dispersion. MAFOR is 0-dimensional aerosol box model which can compute aerosol dynamics and gas phase and aqueous phase chemistry [27]. Note that the model dimension of MAFOR is different from GRAMM/GRAL, which generated the aerosol dispersion plumes in 3-dimension grid system. MAFOR model only calculate the physio-chemical processes of aerosol dynamics with the given aerosol concentration and model set-up (i.e., initial condition for particle size distribution, meteorological data, model configuration to control enable/disable certain processes in the simulation). The performance of MAFOR has already been evaluated in various studies. It was applied to estimate the influence of the aerosol processes on PN concentration in urban areas [45], to explore the formation of particles by the nucleation mechanisms in the exhaust of a diesel engine [46], and to simulate

the formation of nano-particles in the Arctic areas [47]. In the current study, MAFOR model considered the following aerosol dynamics processes: wet particle deposition, Brownian coagulation, dilution with background particles, Kelvin effect, and condensation (of vapors, H_2SO_4, organics, and water). As a result, the model generated time-dependent particle size distributions which allowed to calculate the effect of aerosol aging on the PN concentrations.

Four meteorological variables (relative humidity, temperature, precipitation, and wind speed) and the initial particle size distributions were determined before calculating the aerosol dynamics. Among the meteorological variables, relative humidity, temperature, and precipitation were applied to determine the dynamics of wet particle deposition, coagulation, condensation, and kelvin effect. Wind speed was utilized to calculate the distance how far aerosols travel at a given time. The initial condition for the particle size distribution of the aviation emission was determined by the emission indices measured in LAX airport [34]. The measurement examined 275 sampled plumes during the flight's take-off phases and produced log-normal fit coefficients for particle number and volume size distributions. The geometric mean diameters and their standard deviations from all sampled plumes were used to develop the initial aerosol distributions of the Aitken mode, and the accumulation mode in MAFOR [48].

Moreover, the background ambient condition was also included in the model to consider the effect of other atmospheric pollution sources on the aerosol dynamics. Since no observation data of background ambient PN concentrations in the Zurich area was available, a support vector machine (SVM) model to estimate the background PN concentration from observations at another location was developed. The SVM model was devised in the previous study [23]. The model was trained using the hourly-resolution PN concentration from the Basel Binnigen station of the Swiss National Air Pollution Monitoring Network (NABEL), which is located 1.2 km from the Basel city center and 4 km from the Basel-Mulhouse-Freiburg airport. It was discovered that the measured PN concentration was not changed by the dramatic reduction of aircraft activities during the COVID-19 pandemic, implying that the station experiences only minor influence from the airport [23]. After the training, the SVM model predicts the background PN concentration of the Zurich area with four meteorological variables (temperature, relative humidity, wind speed, precipitation). The particle size distribution of the ambient background condition was taken from a former study on UFPs in the Zurich area [49].

To couple the 3-D dispersion plume from the GRAMM/GRAL and 0-D aerosol dynamics model, it was important to determine the initial PN concentration of the aviation emission to calculate the aerosol dynamics and the coefficient for computing the dilution effect of background ambient particles. In the current study, both values were taken from

the centerline of each plume case taken from GRAMM/GRAL. At first, the dilution of air-traffic emission plumes by the background particles was approximated by fitting a power-law function, $y = a \times x^{-b}$ (where x is distance, $x = u \cdot t$, with wind speed, u, and time, t, and y is concentration) [48]. The plume centerline was defined as the 95 % percentile concentration on the arc concentric with the airport perimeter (the place within 1.5 km from the airport center, 47.27° N, 8.33° E, 432 m.a.s.l) [23] (see Figure 3). Based on this, the PN concentration of the plume centerline was chosen as a representative of the plume. This centerline fitted to the dilution curve of the power-law function and produced the dilution coefficient. Initial PN concentration for MAFOR was taken from the crossing point of the plume centerline and the airport perimeter.

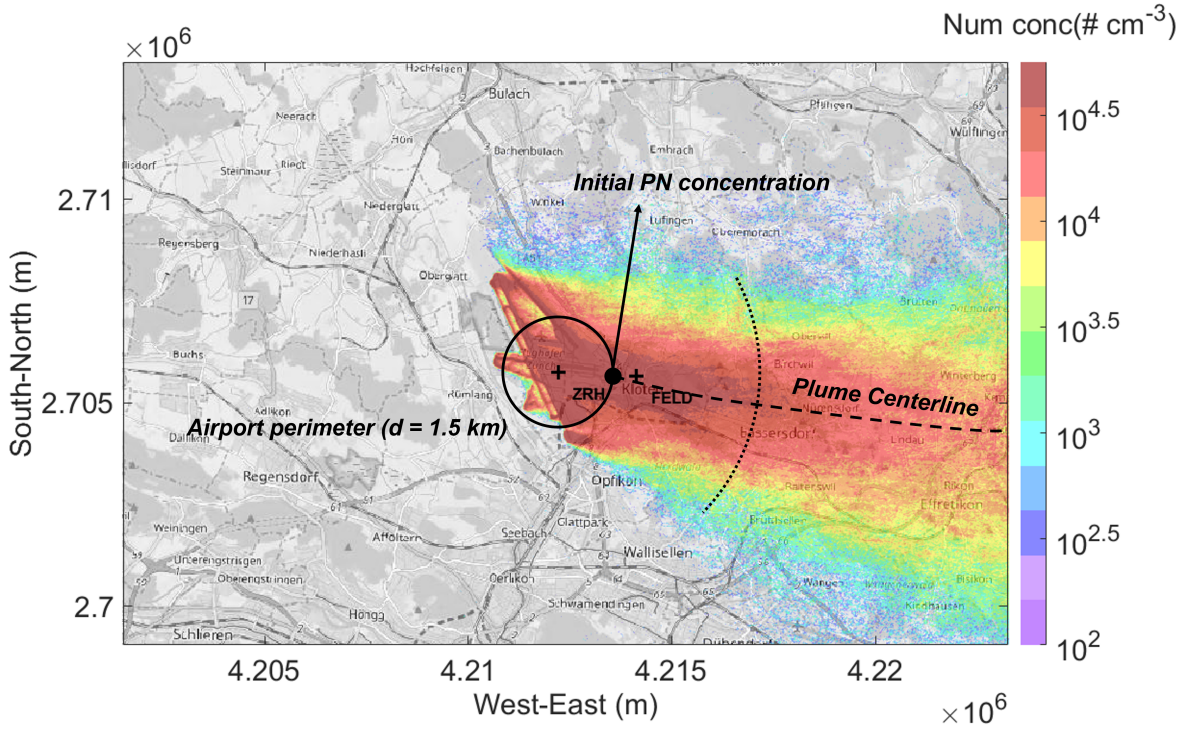

Figure 3: An example of the PN emission plume generated by GRAMM/GRAL and included aerosol dynamics by MAFOR (2019-09-17, 17:00:00). The figure illustrates the location of the airport center (ZRH) and the monitoring station (FELD), as well as the airport perimeter and the plume centerline. The reference coordinate system shown on the x and y-axis is ETRS89-extended / LAEA Europe (EPSG:3035).

3 Results and Discussion

3.1 Particle number emission inventory

3.1.1 Total annual emission

The annual PN emissions for different flight phases were presented in Figure 4. Among the different phases, the PN emitted during the taxiing periods was dominant in both

years, accounting for about 76.6 % ($1.60 \pm 0.65 \cdot 10^{24}$ [particles/year]) of the total PN emission in 2019 and 66.5 % ($4.78 \pm 1.94 \cdot 10^{23}$ [particles/year]) in 2020. In both years, the emission phase contributing least to total emissions was climb-out, only accounting for 1.69 % and 1.87 % in 2019 and 2020, respectively. Note that the PN emission for the climb-out and approach phase in the present study might were limited to the relevant spatial domain of the flight trajectory data and do not represent emissions during each complete phase. Depending on the flights, the climb-out and approach phase can exist outside this regional scope. Overall, $2.09 \cdot 10^{24}$ [particles/year] were emitted from the aircraft at Zurich airport in 2019, which was about four times larger than the PN emission in 2020, $4.78 \cdot 10^{23}$ [particles/year]. Table 1 demonstrated that the total number of flights in 2020 was dramatically reduced compared to the previous year, undoubtedly because of the lock-down policies in Switzerland due to the COVID-19 pandemic situation. Interestingly, the reduction in the aircraft traffic was about 60 %, whereas the reduction of the PN emission was nearly 80 %. A possible reason for this disagreement between the reduction in traffic and the PN emission is that the decreasing number of flights was primarily due to fewer large, commercial (listed) aircraft (see Table 1). Unlisted flights were usually small jets for private or business purposes, and their reduction from 2019 to 2020 was only 12.3 %. On the other hand, the listed flights decreased by 65.8 %. Moreover, the statistics report [30] pointed out that the most significant decrease among Airbus models was for the largest flight type, A380, reduced by 77.2 % compared to the previous year. Airbus accounted for the largest portion in Zurich airport. Hence, it is implied that the size of aircraft types was a significant factor in the stronger reduction of PN emission as compared to plain flight numbers.

Uncertainties of annual PN emissions were calculated by error propagation using the Monte-Carlo approach [50], which was adapted from the previous study [23]. Uncertainty from the ADS-B data was neglected, as the previous study by Zhang et al. [23] stated that its uncertainty could be only a level of several meters. Nevertheless, uncertainties in calculating fuel consumption from the EEA LTO calculator and factors from $EI(\cdot)$ were assessed. Firstly, a measurement study at Zurich airport found that the difference between the actual fuel flow rates of the aircraft engines and their certification values were mostly within 20 % [51]. Therefore, the uncertainty factor for the mass of fuel burnt was set as a normal distribution $f_{fuel} \sim N(1, 0.2/1.96)$, which would multiplied to the estimated $M^*_{fuel,hourly}(p, t_{id})$ during the Monte Carlo simulation. Secondly, the uncertainty factor for the PN emission factor was set as a log-normal distribution $LN(f_{EI}) \sim N(1, ln(2)/1.96)$ by comparing the engine emissions of A320 aircraft types and B737 aircraft types in the previous study [23]. As a result, the standard deviations of estimating the annual PN emission for each flight phase were illustrated in Figure 4. The Monte-Carlo approach quantified the overall uncertainties of the annual PN emission (regarding all flight phases)

can be approximately 80 % (at minimum) to 320 % (at maximum) of the mean values, in both 2019 and 2020.

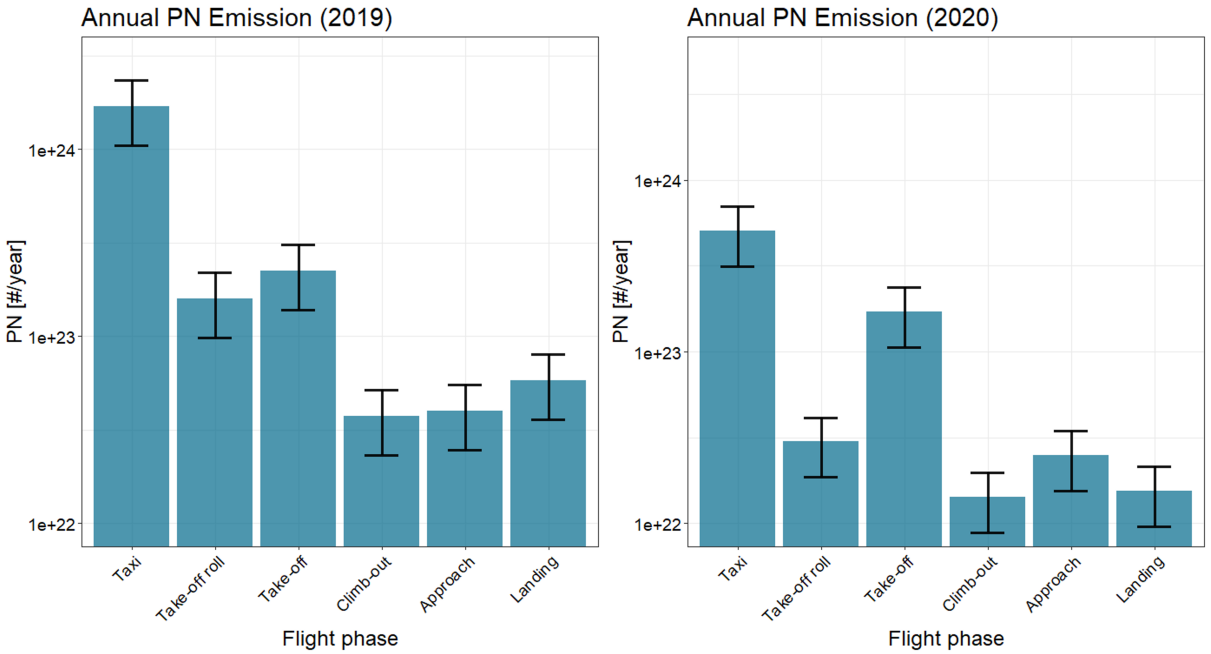

Figure 4: Total PN emissions of different flight phases for the year of 2019 and 2020. The error bars depict the uncertainties of the PN emission estimation derived from the Monte-Carlo method.

The dominance of the taxiing periods in the annual PN emission was primarily due to the longer duration of the taxiing period compared to the other flight phases (see Table 4). The taxiing period in 2019 was 11.9 times longer than the summation of other phase periods and 8.6 times longer in 2020. Indeed, the estimation of taxiing time measured in Zurich airport for a single flight movement was about 18 minutes, while all the other phases are less than 5 minutes [51]. To examine the average PN emission rate, the total annual PN emissions were divided by the total annual duration and the results presented in Figure 5. The average emission rates demonstrated that the PN emission rate was mainly depend on the thrust level of the aircraft engines. The PN emission during the higher thrust level (100 % for take-off roll and take-off, 85 % for climb-out) was 4 - 10 times higher than that during the lower thrust level (7 % for taxi, approach and landing).

Table 4: Total annual duration [hours] of the flight activities for each phase and total number of flights per year. The duration and the number of flights were calculated from the ADS-B flight trajectory database.

Year	Taxi	Take-off roll	Take-off	Climb-out	Approach	Landing	Total ADS-B flights
2019	39613.87	711.96	846.03	94.48	751.08	907.20	253,670
2020	10537.55	179.19	428.23	31.50	326.54	256.65	111,511

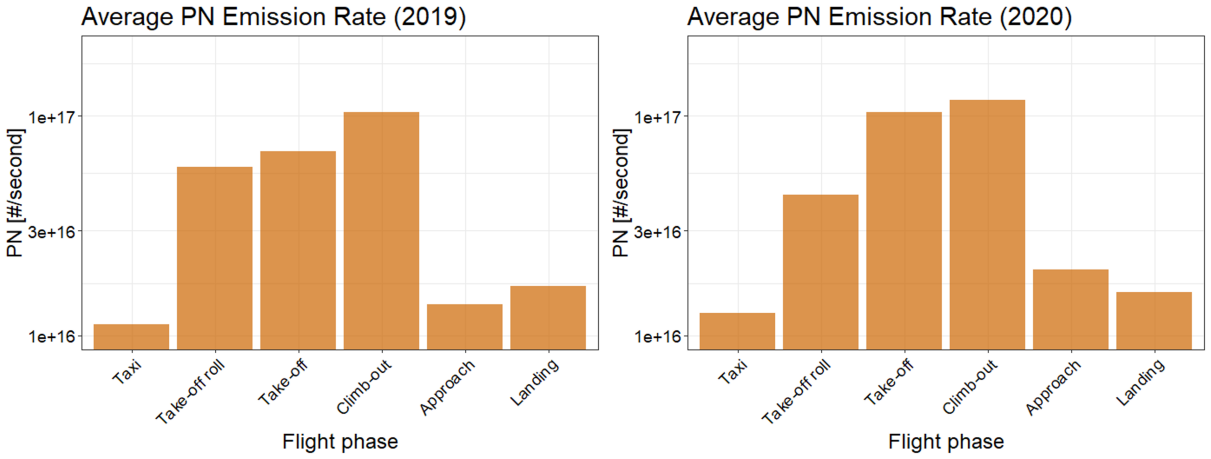

Figure 5: Average PN emission rate of different flight phases for the year of 2019 and 2020. The average values were obtained by dividing the total annual emissions with the annual duration.

3.1.2 Temporal and spatial distribution of the aviation emission

Before the first wave of the COVID-19 pandemic in 2020, Zurich airport emitted on average $1.74 \cdot 10^{23}$ [particles/month] (see Figure 6). PN emissions drastically decreased during the first and second wave of the COVID-19 pandemic, with only $1.10 \cdot 10^{22}$ [particles/month] emitted in April 2020 and $1.75 \cdot 10^{22}$ [particles/month] in October-December 2020. The variation in the aviation emissions would significantly affect the PN concentrations and the particle size distributions in the vicinity of the airport. The observation study [19] identified that the PN concentration when the wind blows from the direction of the airport, diminished by one-sevenths during the first wave, although this reduction in the monitoring station were compensated by the relatively less reduced road-traffic emission. The observation analysis of particle size distributions also showed a large reduction in particles with diameters less than 20 nm during the same period.

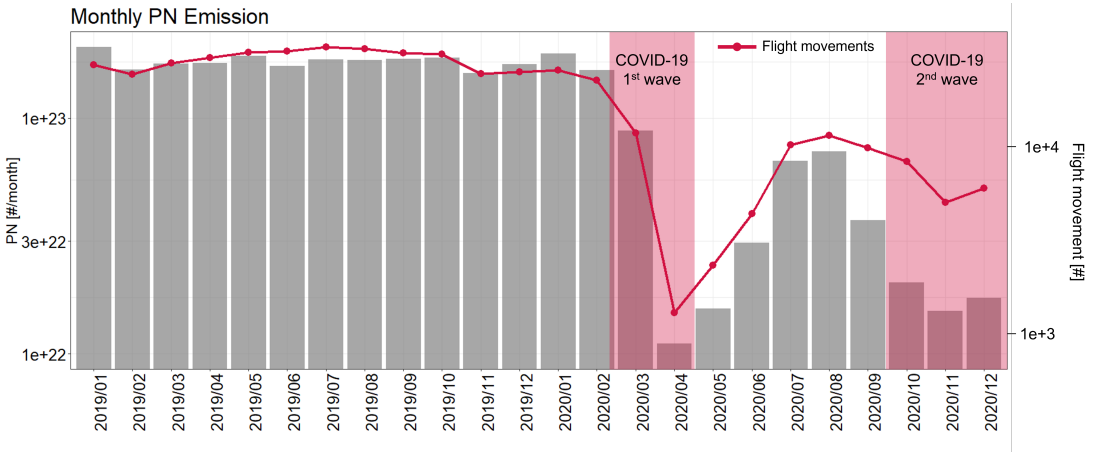

Figure 6: Monthly distribution of the PN emission and the flight movements at Zurich airport in 2019 and 2020. The period of the first and second waves of the COVID-19 pandemic for Switzerland is defined here as 2020.02.26 - 2020.04.30 and 2020.10.01 - 2020.12.31, based on [52].

In addition, diurnal variation of PN emission is depicted in Figure 7. Due to the noise protection regulations in Zurich airport, regular flights are not permitted between 0:00 and 6:00 local time [29]. No difference among the seasons was present in 2019, whereas substantial seasonal differences were found in 2020 due to the COVID-19 pandemic. The temporal variation and its effect on the simulation results is assessed in Section 3.2 and 3.3.

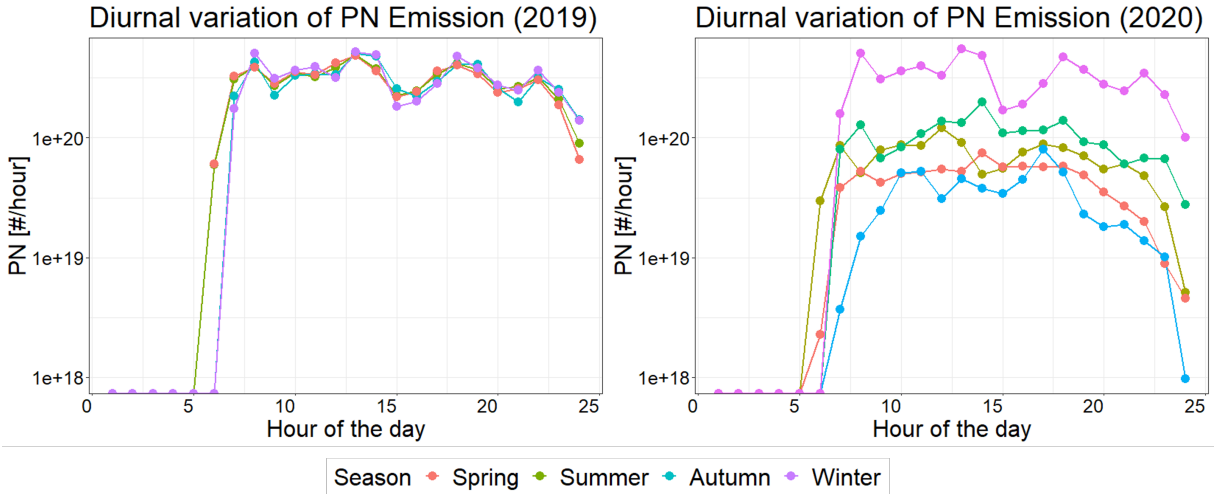

Figure 7: Diurnal variation of PN emission in 2019 and 2020. The variation was averaged for each season of the year, which was partitioned into spring (March to May), summer (June to August), autumn (September to November), and winter (December to February). In 2020, winter was divided by the season before (January and February) and after (December) COVID-19 pandemic period.

Based on the ADS-B flight trajectories, annual spatial distributions of the PN emissions were obtained for different flight phases as shown in Figure 8. The distribution was derived on a 5 m $\times$ 5 m grid covering the airport and adjacent areas. The spatial distribution confirmed that the flight trajectory database provides highly accurate geo-located data. The distributions for the taxiing period, Figure 8(a) and (c), precisely captured all runways and taxiways at Zurich airport. It is found that the flight trajectory data could provide sufficient information to specify emission hot-spots inside the airport. Following the previous study [23], the push-back areas, where the flights are moved by ground-service vehicles instead of using their own engines to protect the airport facilities from their emissions, were considered as no emission areas. Moreover, the emissions in take-off periods were depicted as Figure 8(b) and (d), and they indicated the main routes of flight take-offs at Zurich airport. The distribution of the all phases including the emission distributions and their hot-spots are provided in the Appendix A2.

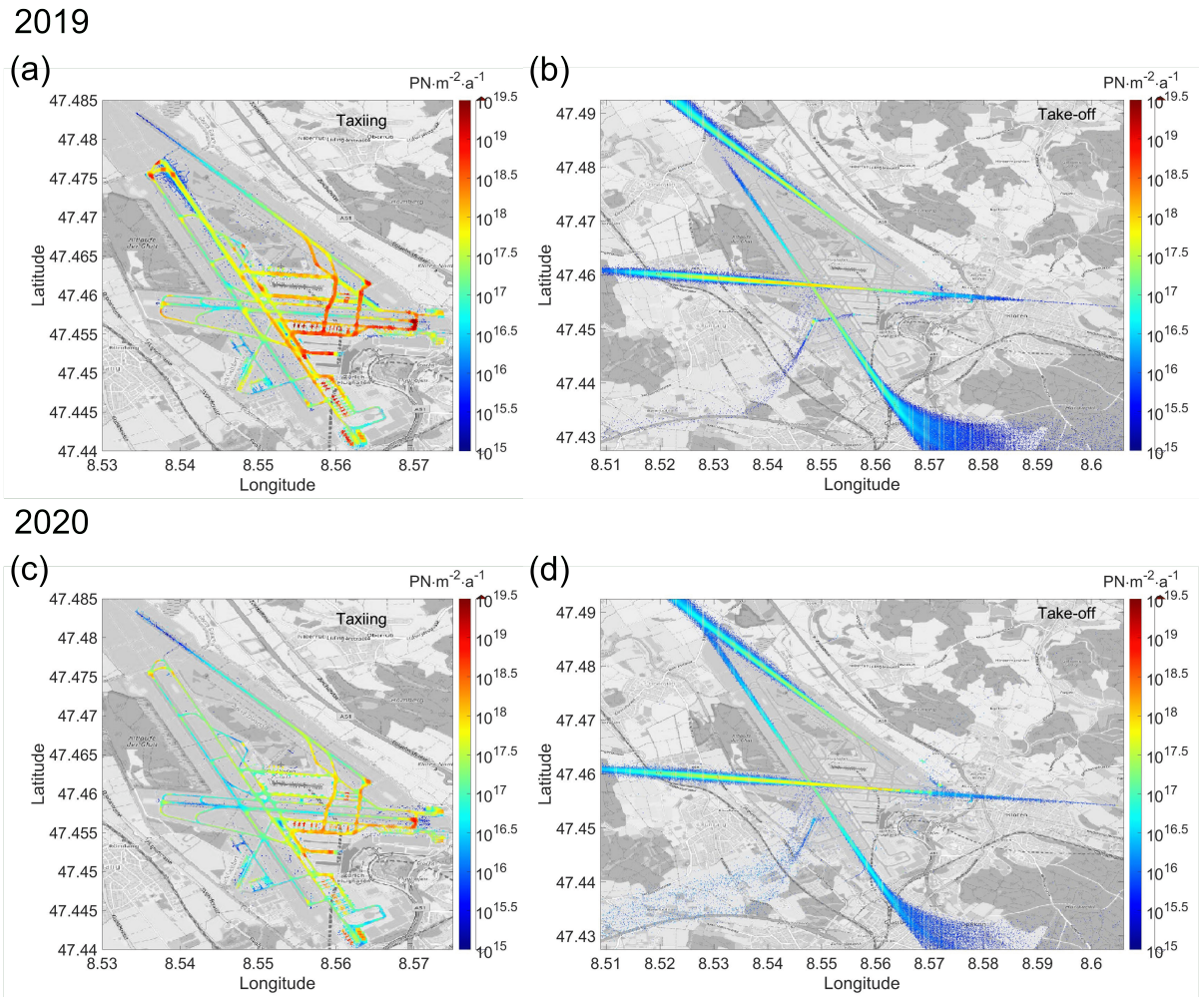

Figure 8: Spatial distribution of the PN emission in 2019 and 2020. Among the six flight phases, the emission during taxiing periods, (a) and (c), and during take-off periods, (b) and (d), are presented. The reference coordinate system shown on the x and y-axis is WGS 84 (EPSG:4326).

3.2 Estimation of particle number concentration

3.2.1 Aerosol dynamics on particle number concentration

Aerosol dynamics are of importance in quantifying the number of airborne particles. Due to their small particle sizes, the UFPs emitted by aviation tend to quickly coagulate when the particles interact with each other and with background particles, overall leading to a decrease in PN concentrations [23]. It should be noted that the amount of PN emissions and background particles can substantially affect the coagulation. However, due to the computational costs the current study only explored the aerosol dynamics at the plume centerline when coupling the GRAMM/GRAL and MAFOR models. In addition, it was assumed that aerosol dynamics in regions outside of the plume centerline would be the same as simulated for the centerline, leading to the same relative decrease in PN concentrations. However, the assumption might provide additional errors in calculating

the PN concentrations at, for example, the monitoring station. Figure 9 demonstrates the dilution of the particles from aircraft emissions in the plume centerline with or without considering aerosol dynamics. The effect of aerosol dynamics, as simulated by MAFOR, can be examined by the difference between two lines in Figure 9(b). The figure depicts that at a distance of 30 km away from the airport, PN concentrations dropped 4-fold when considering the aerosol dynamics as opposed to inert particles. However, the impact of aerosol dynamics was dependent on the duration that particles need to reach a certain location from the initial condition at time of emission. Therefore, the average wind speed within the plumes plays a critical role in the influence of aerosol dynamics on PN concentration at a given location/distance from the airport. The monitoring station near Zurich airport (FELD in Figure 9(a)) was located about 419 m away from the airport perimeter (1919 m from the airport center). The former example of MAFOR calculations implies that only a small influence of aerosol dynamics can be expected at this location because the relatively short distance between the station and the airport, which would not be sufficiently long for considerable aerosol aging. Therefore, the study considered the distance from the airport center (1919 m) when calculating the effect of aerosol dynamics at the location of the monitoring station, even though the initial PN concentrations for MAFOR were taken from the airport perimeter. The influence of aerosol dynamics on the hourly-resolution PN concentration was also presented in Section 3.2.2.

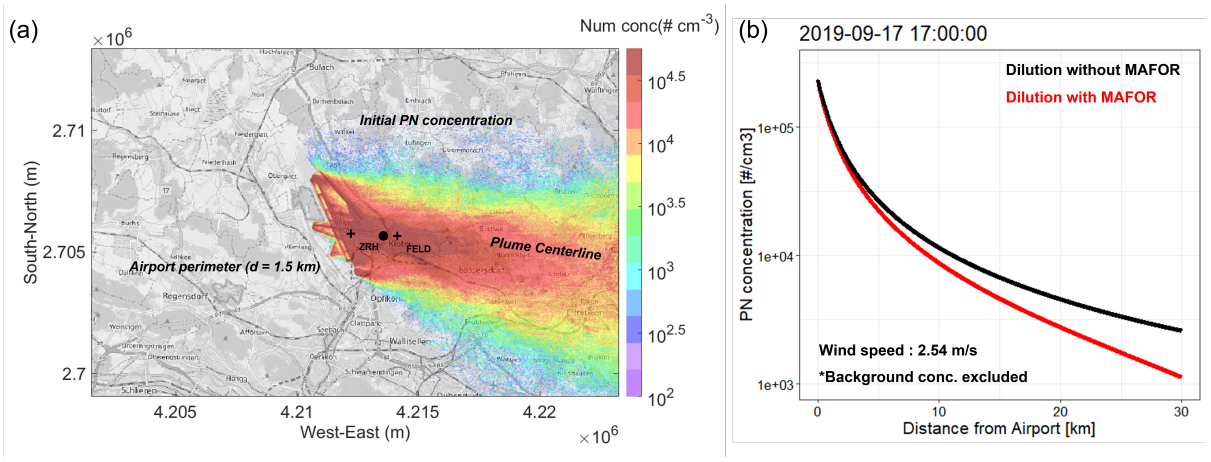

Figure 9: The consequence of aerosol dynamics calculated by MAFOR. The figures described the effect of MAFOR on PN concentration in a specific hour (2019-09-17, 17:00:00). (a) illustrates the location of the airport center (ZRH) and the monitoring station (FELD), as well as the emission plume, airport perimeter, and the plume centerline in the period. Figure (b) demonstrated PN concentrations in the plume centerline with or without considering the aerosol dynamics.

Moreover, Figure 10 describes the spatial distribution of the annual mean PN concentrations caused by aviation emissions in the vicinity of Zurich airport in 2019 and 2020. Despite the significant difference in the aviation emission in 2019 and 2020 due to the COVID-19 pandemic lock-downs, Figure 10(b) points out that the air-traffic emissions in

2020 still strongly impacted the annual mean PN concentrations at the monitoring station (FELD) by $6.32 \cdot 10^4$ cm^{-3}, although this was one-third of the value in 2019, $1.82 \cdot 10^5$ cm^{-3}. The differences in the influence of aviation emissions between the two years increased as the location was more distant from the airport. For example, the aviation emission also reached the city center of the Zurich, yet the concentration increased only 10^3 to $10^{3.5}$ cm^{-3} in Zurich main station (Zurich HB in Figure 10). This level of influence was lower than typical background PN concentrations of Zurich city center, which were previously measured as $2 \cdot 10^4$ cm^{-3} [53].

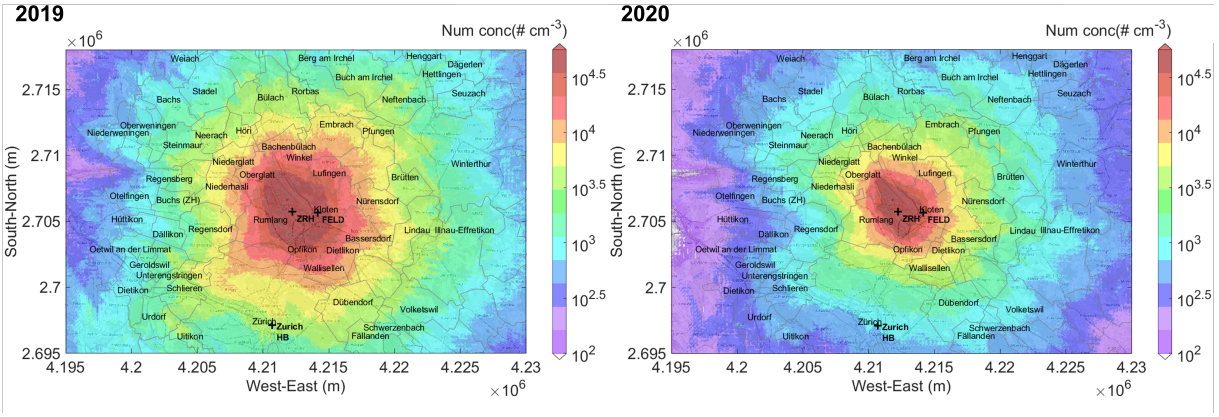

Figure 10: Annual spatial distribution of the PN concentrations in 2019 and 2020. The concentration was only derived from the aviation emission and excluded the background concentration, and it was taken at the level of 2 m above the ground. The location of the airport center (ZRH), the monitoring station (FELD), and Zurich main station (Zurich HB) are labeled in the figures. The reference coordinate system shown on the x and y-axis is ETRS89-extended / LAEA Europe (EPSG:3035).

3.2.2 Comparison between the simulation and observation

The observed PN concentration only captured the particles with dynamic diameters between 10 nm and 100 nm. In order to compare them to model simulations, the latter were refined to obtain PN concentrations in the same size range. MAFOR produced time-dependent particle size distributions, which demonstrated the evolution of size distribution by aerosol dynamics for every 10 seconds from the initial conditions. Considering wind speeds and the distance between the airport and the monitoring station (1919 m), particle size distributions were taken from the period when the emitted particles reached the monitoring station. The simulated distributions were recorded in 120 bins of particle diameter in the range from 1 nm to 2500 nm. The values in the bins ranging from 10 nm to 100 nm were considered to calculate simulated PN concentrations that can be compared directly to the observations. The comparison between the simulated and measured PN concentration is illustrated in Figure 11 and 12. Moreover, the shares of PN emission from each flight phase, which quantified how much they influenced the simulated PN concentrations in each year, were presented in Appendix A3.

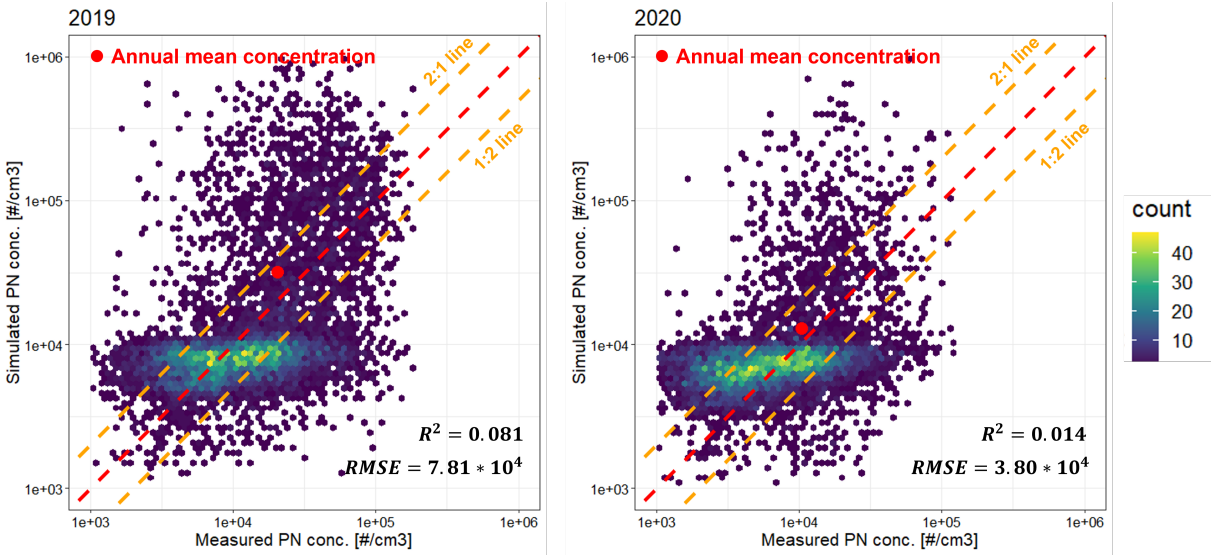

Figure 11: Scatter plots of simulated hourly PN concentrations from the models versus the measured hourly PN concentrations from the monitoring station in 2019 and 2020. A heat map was presented to illustrate the distribution of scatter points in the plots. In addition, the annual mean PN concentration was given as a red dot.

Zhang et al. [23] compared the simulated annual mean PN concentrations at four locations in Zurich airport area against observations. They found that simulated annual mean concentrations were within a factor of 2 of the observed values. Here, the annual mean concentrations at the measurement site in Kloten are compared separately for 2019 and 2020. Similar to the previous study, good agreement for the annual means was established. Both observed and simulated PN concentrations were lower in 2020 than in 2019. Although meteorological factor may have been responsible for these lower concentrations, it seems likely that they reflect the impact of the COVID-19 pandemic and that this impact is captured correctly in the model.

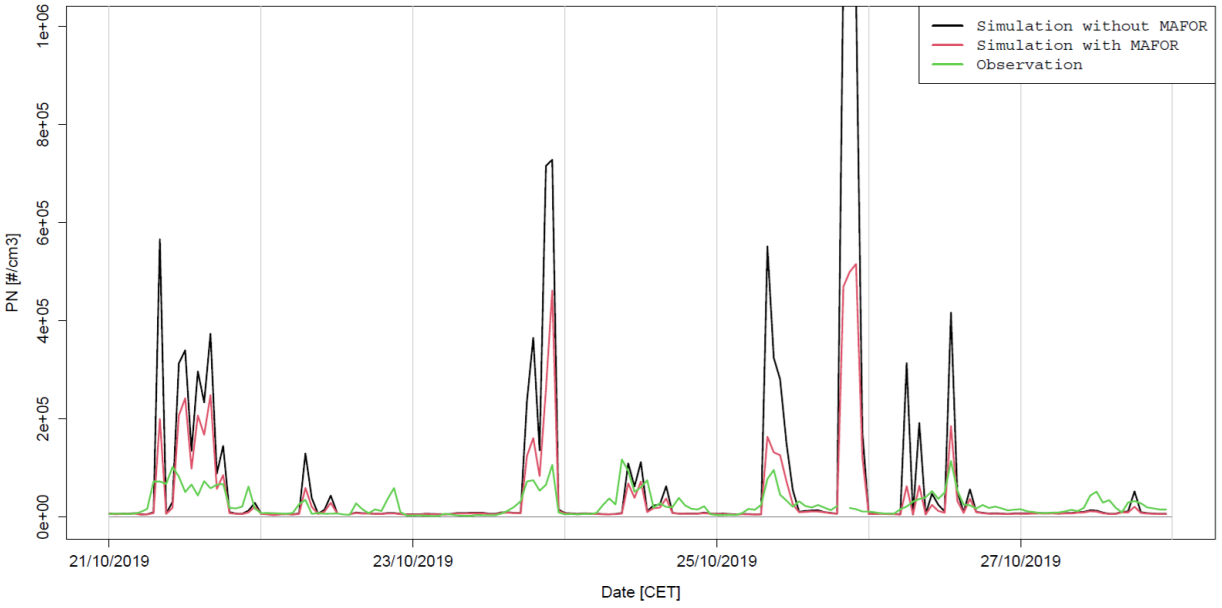

Figure 12: An example of the time-series of hourly PN concentrations in 2019-10-21 to 2019-10-27. Measured PN concentrations (Observation), simulated PN concentrations without aerosol dynamics (Simulation without MAFOR), simulated PN concentrations with aerosol dynamics (Simulation with MAFOR) are depicted.

When comparing hourly mean PN concentrations, the time-series in Figure 12 demonstrated that the coincidence of peak locations between the simulation and the observation was generally corrected. This peak coincidence pointed out two important features: (1) GRAMM/GRAL reproduced the atmospheric transport from the airport qualitatively well, and (2) the aviation emission were largely responsible for the PN concentration peaks. The coincidence of the peak locations were utilized to evaluate the model performance quantitatively. Since the observation analysis concluded that the PN concentration increased 2-4 fold when the wind blew from the airport [19], a criterion to classify peaks of PN concentration was defined as the values which are four times higher than the estimated background concentration. Figure 13 illustrates the confusion matrix of peak classifications. Overall, 49.3 % of the observed peaks were coincident with the simulation in 2019, whereas only 25.0 % in 2020. The weaker coincidence in 2020 is thought to be mainly due to lower aviation emissions and the relatively strong impact of road emissions on the measurements. The simulations did not consider road-traffic emissions at all. However, a majority of the data points were classified as 'Non-peak' in both simulations and observations, which may indicate that the criterion disregards a considerable number of smaller peaks. The current methodology regarded as a simple method to evaluate the peak coincidence. Developing a more sophisticated way to evaluate the simulation peak coincidence could be helpful in further analysis. For example determine under which atmospheric conditions peaks are either missed or wrongly predicted by the simulation.

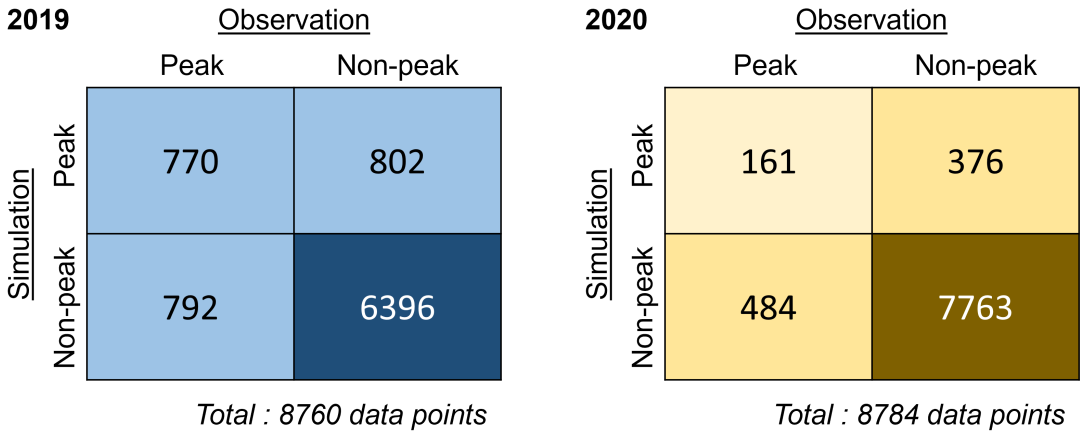

Figure 13: The coincidence of the peak locations between the simulation and the observation in 2019 and 2020. 'Peak' was defined when the hourly PN concentration was four times higher than the estimated background concentration, and 'Non-peak' for the other periods.

Hourly mean PN concentrations also illustrated that little correlation between measured and simulated results can be seen in either years (see Figure 11). It is speculated that there are three main limitations of the model that may explain the lack of consistency.

First, the estimation of the background concentration by the SVM model, in which the values were utilized for MAFOR, could not reproduce the variation of the background concentration shown in the measurements. This aspect is manifested in Figure 11 as horizontal clouds in the heat maps, where the simulated PN concentration was around 10^4 cm^{-3}, while measured PN concentrations range roughly from 10^3 to 10^5 cm^{-3}. This can be seen even more clearly in the scatter plots of the estimated background concentration without the aviation emission, as presented in Appendix A4. The estimation approach to the background concentration was developed by training the SVM model with the PN concentration and meteorological data from the Basel Binnigen station of the NABEL network. The rational for using data from the Basel station for the model training was that: 1) the station was located in a similar environment as the FELD station, and 2) that the site was not affected by aviation emission. Indeed, the annual mean background concentration represented a good prediction. Nevertheless, the model might not be utilized to examine the hourly averaged values. A possible explanation for the deficiency is that the meteorological variables to estimate the PN concentration would not provide sufficient information to predict the variation of PN concentration at a different location than that of the original training dataset. NO_x concentrations were included as predictor variables in the former study [23]. However, it was excluded in the present study because NO_x also emitted from the air- and road-traffic emission and its impact on the background concentration was deemed a source of error when included as predictor variable. Re-evaluating the current variables and investigating additional variables (i.e., stability class, mixing height) would be beneficial to implement a better prediction with the SVM model.

Second, the simulation over-estimated the PN concentrations, especially peak values. The difference in the peak periods was illustrated in an example of the concentration time-series in Figure 12. The time-series of other periods can be found in the digital supplementary materials. The simulation peaks were 2-10 times higher than the observation peaks despite the decreases predicted by the aerosol dynamics model. The PN emission factor (see Equation 4) could potentially cause the over-estimation. The factor originated from the regression model developed by two studies: measurement of take-off engine emissions in LAX airport and NASA's laboratory experiment on jet fuel composition. On the one hand, the field measurement in LAX airport was implemented 400 m away from the runways [34]. Hence, background particles near the airport can be quantified together with the jet engine emission. Moreover, the measurement only considered 253 plumes of the flight take-off in LAX airport, whereas it was reported that the total number of flights in LAX airport was 691,257 in 2019 and 379,364 in 2020 [54]. The sampled plumes might not be sufficient to comprehend the emissions from the diverse aircraft types and to apply their results to Zurich airport. The higher ambient temperature in LAX airport than in Zurich airport might also affected to the over-estimation. On the other hand, the NASA experiment examined the PN emission with 15 different fuels with various percentages of sulfur content, total aromatics, naphthalene, and hydrogen, but they only implemented it with a single engine type, CFM56-2-C1 [33]. Even though this engine is typically used by the Airbus A320 and Boeing 737 families, which accounted for 33.2 % of total flights in 2019 and 34.3 % in 2020 in Zürich, it might not be representative for the whole fleet at Zurich airport [29; 30]. It was identified that 49.4 % of the flights in 2019 and 43.6 % of the flights were aircraft smaller than A320 and B737 families. Thus, using data from the NASA experiment could produce an over-estimation in quantifying the PN emission. An ultimate approach to converting the mass of fuel burnt to PN emission of an aircraft has not yet been established, and there was no such standard that yields satisfactory results. Nevertheless, the empirical relations in the current study were applicable to distinguish the levels of the emission impact at a certain location in the near-airport regions. A further study to quantify the PN emission by considering other factors would increase the accuracy of the estimation of the aviation emission.

Lastly, the simulated PN concentrations only examined the particles from aviation and background conditions, but excluded road-traffic emissions. The FELD station was close to the motorway A51 (about400 m west of the station). Hence, road-traffic emissions may dominate observed PN concentrations when aviation emissions are either small (night, lockdown) or did not reach the monitoring site (wind direction). Figure 12 illustrates some periods where clear peaks were present in the observations but not in the simulations, as also indicated by Figure 13. Furthermore, the spatial distribution applied to GRAMM/GRAL did not consider hourly variations in the emission patterns as they

would occur in reality. The annual spatial distribution was utilized for the area sources of the dispersion model, and only the temporal distribution of the flight activities was considered to develop the hourly-resolution PN concentration. Since the monitoring station was close to the airport, the observed PN concentration would be sensitive to the true location of the aviation emissions. The aircraft types also largely influence the PN emissions, though the current study did not consider the different types of aircraft in each hour, but assumed the same average fleet at all times. Developing the dispersion model with an hourly spatial resolution of PN emissions specific to actual filght data would likely increase the model's performance. However, it would come at larger computational costs and would require obtaining a complete dataset of all flight activities.

3.3 Estimation of particle size distribution

3.3.1 Aerosol dynamics on particle size distribution

Figure 14 presents the impact of aerosol dynamics on the particle size distribution for two different environmental conditions. Figure 14(a) was obtained when the estimated PN concentration at the field site was a high peak ($1.82 \cdot 10^5$ cm^{-3}) and the wind blew from the airport (wind direction 300°), and Figure 14(b) was taken from the first COVID-19 lockdown period in 2020 when aviation emissions hardly influenced the station. Wind speeds were considered sufficiently large for aircraft emissions to reach the monitoring station when selecting periods for the comparison. In the figures, the 'Initial' condition of the distribution was taken from the airport perimeter, which gave the initial PN concentration to MAFOR. Moreover, 'Distance' indicated the distance between the initial condition and specific locations along the plume centerline.

From Figure 14(a), it can be seen that particles with a diameter between 10 and 30 nm contributed a considerable fraction of total PN concentrations when large influence from aviation emissions was presented. These particles were also significantly influenced by aerosol dynamics, as the concentrations decreased 10-80 folds by the time the particles had traveled about 10 km. The reduction could be caused by the coagulation processes by MAFOR between the particles of nucleation and Aitken mode [48]. On the contrary, particles with a larger size ($D_p > 100$ nm) were not affect a lot by coagulation. Indeed, their concentrations were getting slowly larger as the distance increased, which again is the result of coagulation of smaller particles. Figure 14(b) illustrates particle size distributions when the impact of aviation emissions was negligible. In general, the background distribution profile dominated in all distances, and the concentrations increased as the particles were distant from the airport. Overall, the difference between Figure 14(a) and (b) clearly illustrated the impact of aviation emissions on the particle size distributions as well as the importance of the aerosol dynamics especially in the case with fresh particle

emissions.

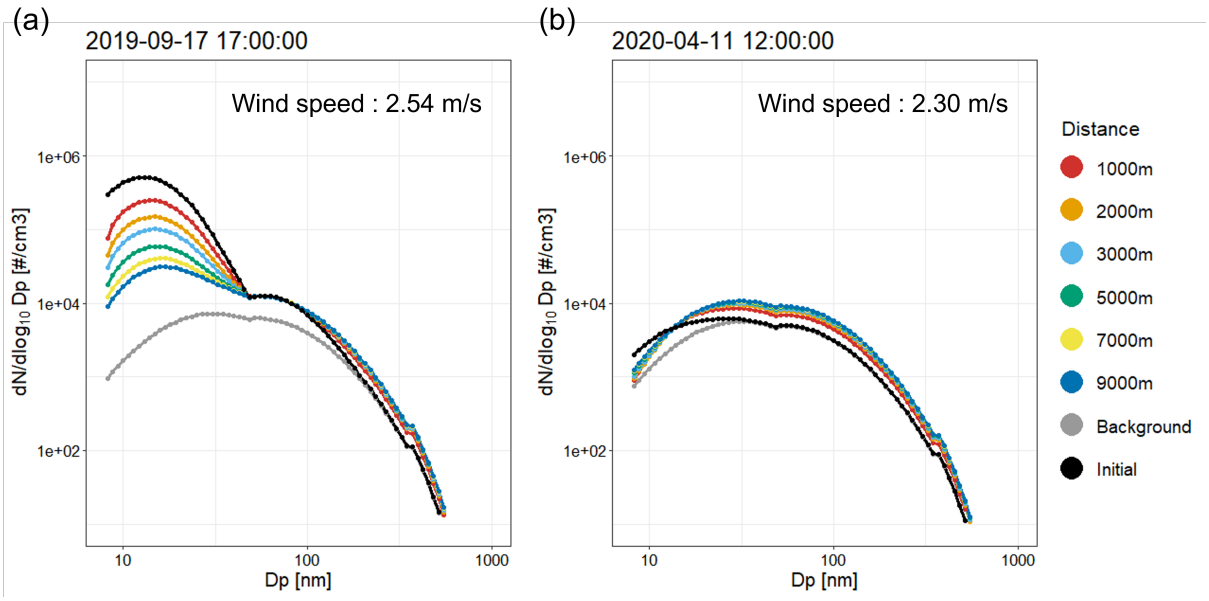

Figure 14: Two examples on the evolution of particle size distributions at the plume centerline at (a) 2019-09-17, 17:00:00 and (b) 2020-04-11, 12:00:00. The simulated PN concentrations from aviation emissions (excluding the background particles) were (a) $1.82{\cdot}10^5$ cm^{-3} and (b) $4.70{\cdot}10^3$ cm^{-3}, respectively. Particle size distributions in the figures included both aviation emissions and background particles.

3.3.2 Comparison between the simulation and observation

Figure 15 presents the comparison of simulated and observed particle size distributions averaged for three different time intervals: daily, monthly, and yearly. In the comparison of hourly PN concentrations in Figure 11, it was identified that evaluations of the simulation performance could be contrasted by looking into the different mean values. Thus, an intention of exploring the distributions in various intervals was to examine the simulated particle size distributions through multiple aspects and not simply assess its performance with a single average profile. In general, all simulated particle size distributions illustrated the same shape of the distribution with two maxima around 15 nm and 65 nm because a bimodal distribution from the log-normal fit coefficients was identically applied for all initial conditions for the MAFOR calculations. The simulation was based on a robust assumption that initial distributions are determined in both the aviation emission and the background particles. On the contrary, the observed particle size distribution depicted a more linear distributions. The linearity was primarily due to the averaging effect of different hourly distributions with varying modal means. Since observed size distributions did not have a fixed modal diameter, the linearity of the mean spectrum results from averaging over distributions with different modal means. From the observed distributions, it was pointed out that the linearity enhanced when the time interval for the averaging increased.

Figure 15(a) and (b) shows examples of particle size distributions from a day when high and low PN concentrations were measured at the monitoring station, respectively. The investigated days were selected based on the daily-averaged PN concentration, flight movements, and meteorological conditions. The day with high PN concentrations (2019-10-21) had a daily mean PN concentration of 42,038 cm^{-3} and the wind blew directly from the airport during 7:00 - 23:00 local time. The day of low PN concentration (2020-04-11) was during the first COVID-19 lock-down period, where only 63 flight movements were counted per day [29]. Both the simulations and the observations highlight that the high PN concentration on 2019-10-21 was mainly due to small-size particles (D_P of 10-30 nm) compared to 2020-04-11. The overestimation aspect of simulated PN concentrations was characterized by the distribution of high PN concentration, as the observed distribution did not have a high peak at small particle sizes as the simulation has. Moreover, the simulated distribution of the day with low PN concentration had lower PN at smaller particle sizes than the observation. The difference might be caused by road-traffic emissions, which were not considered in the simulations but affect the observations. Again, road-traffic emissions from the nearby motorway were also an important source of UFPs to the FELD station and would be the biggest source of the PN concentration when the impact of aviation emissions was low or absent. Same of these features were also presented in the monthly-averaged distributions as shown in Figure 15(c) and (d). April 2020 was during the first COVID-19 lock-down period and was the month with the lowest flight movements in two years. The measured monthly average PN concentration in April 2019 was 18,285 cm^{-3}, whereas in 2020 the value was 7,720 cm^{-3}, more than 2 times lower than the values in 2019. Corresponding results from the simulation was 29,816 cm^{-3} for April 2019 and 8,424 cm^{-3} for April 2020, which indicated that aviation emissions were the main cause for the difference in Figure 15(c) and (d).

At last, Figure 15(e) and (f) show average particle size distributions for 2019 separated into two classes: 1) periods when the measurements were expected to be influenced by aviation emissions and 2) periods when aviation emissions were unlikely to reach the monitoring site. Three criteria were applied to distinguish the two classes: (i) wind direction was from the direction of the airport ($210° < \theta < 330°$), (ii) wind speed was higher than 0.5 m/s, and (iii) only the day-time (6:00 - 24:00) distributions were considered, because there were no flight activities during the night-time (00:00 - 6:00) by the airport regulation [29]. As a result, 26 % (2,316 out of 8,760 hours) of the simulated distribution and 23 % (2,037 out of 8,760 hours) of the observed distribution were classified as the 'Influenced' periods, and the rest periods as 'Not influenced'. Same as the other comparisons, the figures indicate the impact of aviation emissions on the distribution of small particles. Nevertheless, the difference between the 'Influenced' and 'Not-influenced' periods was less significant than in other comparisons. A possible reason is that other

PN emission sources largely affected the yearly averaged distribution, while the distribution of 2020-04-11 ('Low PN concentration') and April 2020 were specific periods when human activities were substantially reduced. In addition, when excluding the aviation emission, the background PN concentrations at night-time periods were generally higher than those at day-time periods due to the stable atmospheric boundary layer. Overall, the comparison in Figure 15 indicates that the simulations were able to explain the impact of aircraft emissions on the particle size distribution, showing similar characteristics as the observations. However, one limitation was revealed in that the shapes of the simulated distributions primarily relied on the initial conditions, whereas in reality modal maxima changed with time and averaging resulted in more linear distribution functions.

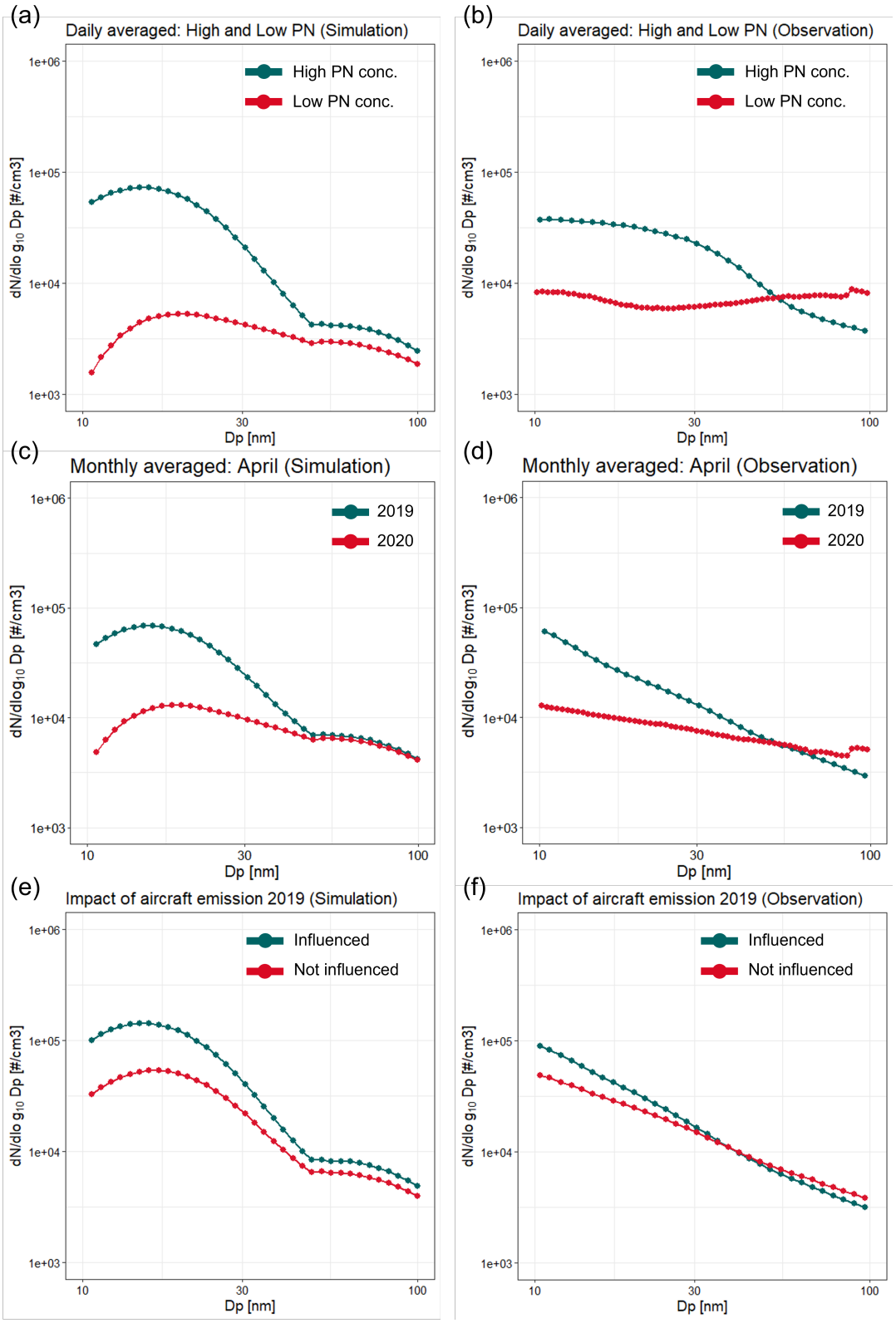

Figure 15: Comparison of the particle size distributions between the simulation and the observation. The distributions were averaged in three different time intervals. (a) and (b) are daily-averaged distributions comparing a day of high PN concentration (observed as 42,038 cm^{-3}), 2019-10-21, and a day of low PN concentration (observed as 7,117 cm^{-3}), 2020-04-11. (c) and (d) are monthly-averaged distributions comparing April 2019 with April 2020. (e) and (f) depicted impacts of the aviation emission on the particle size distribution in 2019 by dividing distributions into 'influenced' periods and the other periods with certain criteria and averaged them accordingly.

4 Conclusion and Implication

The present study investigated the impact of aviation emissions from Zurich airport by developing a PN emission inventory and calculating aerosol dispersion and dynamics for the years 2019 and 2020. In particular, the performance of the model simulations was evaluated against observed hourly PN concentrations and particle size distributions from an adjacent monitoring station. The modeling study intended to distinguish the impact of aircraft emission from other possible emission sources because an observation study alone could not completely rule out the impact of other sources (e.g., road traffic) on observed PN concentrations. The simulations were capable of demonstrating that aviation emissions considerably increased PN concentrations in the vicinity of Zurich airport. A large fraction of the increment was derived from particles with diameters between 10 nm and 30 nm. Nevertheless, the developed PN emission inventory and the model simulations alone may not be sufficient for assessing aircraft emissions, considering that several limitations were detected and disagreements with observations were not fully explained. A significant drawback was found in calculating the hourly-resolution PN concentrations, as the prediction had a poor correlation with the observations (see Figure 11). The scatter plots and time-series implied deficiencies in the methodologies to compute the PN concentrations. In particular, estimation of background concentrations with the SVM model had its limitations and should be improved in future studies. Even more important is the utilization of empirical PN emission factors to convert the mass of fuel burnt to the number of emitted particles. In the absence of other studies, the utilized emission factors were taken from just two studies, the one investigating take-off emissions at the Los Angeles airport and the other by NASA exploring PN emission with diverse fuel compositions, and applied for calculating PN emissions for all taxiing and flight phases. The obtained PN emissions are therefore highly uncertain.

The present study also implies that more and improved input information is needed for enhancing model performance. Both PN concentrations and particle size distributions agreed reasonably on annual average but not for hourly values. In GRAMM/GRAL, only the annual spatial distribution of the PN emission was considered, and the hourly spatial variation on the flight activities and their aircraft types was neglected. This simplification might have contributed to the poor simulation performance, although the computational costs for simulating hourly dispersion profiles would have been to high. In addition, the input for the aerosol dynamic model MAFOR could be improved. For instance, the initial condition for the particle size distribution of aircraft emissions was taken from a study from Los Angeles airport and might not be representative for the conditions at Zurich airport.

In addition to the improvements in the modeling, a comprehensive study on aviation

emissions would achieve a holistic approach to the impact assessment. Ultra-fine particles notably cause adverse health effects by deeply penetrating the human body. Apart from the number concentration and the size of the particles, the composition of the aerosols would also be an important factor in assessing the impact of aviation emissions on human health because the toxicity would be largely varied according to the compositions.

References

[1] Ioannis Nezis, George Biskos, Konstantinos Eleftheriadis, and Olga-Ioanna Kalantzi. Particulate matter and health effects in offices-a review. *Building and Environment*, 156:62–73, 2019.

[2] Jason D Sacks, Lindsay Wichers Stanek, Thomas J Luben, Douglas O Johns, Barbara J Buckley, James S Brown, and Mary Ross. Particulate matter–induced health effects: who is susceptible? *Environmental health perspectives*, 119(4):446–454, 2011.

[3] Weidong Wu, Yuefei Jin, and Chris Carlsten. Inflammatory health effects of indoor and outdoor particulate matter. *Journal of Allergy and Clinical Immunology*, 141(3):833–844, 2018.

[4] HEI Review Panel on Ultrafine Particles. Understanding the health effects of ambient ultrafine particles, 2013.

[5] Kenneth Donaldson, Vicky Stone, Anna Clouter, Louise Renwick, and William MacNee. Ultrafine particles. *Occupational and environmental medicine*, 58(3):211–216, 2001.

[6] Prashant Kumar, Lidia Morawska, Wolfram Birmili, Pauli Paasonen, Min Hu, Markku Kulmala, Roy M Harrison, Leslie Norford, and Rex Britter. Ultrafine particles in cities. *Environment international*, 66:1–10, 2014.

[7] Dean E Schraufnagel. The health effects of ultrafine particles. *Experimental & molecular medicine*, 52(3):311–317, 2020.

[8] C. Loane, C. Pilinis, T. D. Lekkas, and M. Politis. Ambient particulate matter and its potential neurological consequences. *Reviews in the neurosciences*, 24(3):323–335, 2013. Cited By :29.

[9] Maciej Strak, Nicole AH Janssen, Krystal J Godri, Ilse Gosens, Ian S Mudway, Flemming R Cassee, Erik Lebret, Frank J Kelly, Roy M Harrison, Bert Brunekreef, et al. Respiratory health effects of airborne particulate matter: the role of particle size, composition, and oxidative potential—the raptes project. *Environmental health perspectives*, 120(8):1183–1189, 2012.

[10] Brian Stacey. Measurement of ultrafine particles at airports: A review. *Atmospheric Environment*, 198:463–477, 2019.

[11] Judith C. Chow and John G. Watson. Review of measurement methods and compositions for ultrafine particles. *Aerosol and Air Quality Research*, 7(2):121–173, 2007.

[12] M. Gauss, I. S. A. Isaksen, D. S. Lee, and O. A. Søvde. Impact of aircraft no$_x$ emissions on the atmosphere; tradeoffs to reduce the impact. *Atmospheric Chemistry and Physics*, 6(6):1529–1548, 2006.

[13] Isabelle Pison and Laurent Menut. Quantification of the impact of aircraft traffic emissions on tropospheric ozone over paris area. *Atmospheric Environment*, 38(7):971–983, 2004.

[14] MP Keuken, M Moerman, P Zandveld, JS Henzing, and G Hoek. Total and size-resolved particle number and black carbon concentrations in urban areas near schiphol airport (the netherlands). *Atmospheric Environment*, 104:132–142, 2015.

[15] M Stafoggia, G Cattani, F Forastiere, A Di Menno di Bucchianico, A Gaeta, and C Ancona. Particle number concentrations near the rome-ciampino city airport. *Atmospheric Environment*, 147:264–273, 2016.

[16] Shishan Hu, Scott Fruin, Kathleen Kozawa, Steve Mara, Arthur M Winer, and Suzanne E Paulson. Aircraft emission impacts in a neighborhood adjacent to a general aviation airport in southern california. *Environmental science & technology*, 43(21):8039–8045, 2009.

[17] Farimah Shirmohammadi, Mohammad H Sowlat, Sina Hasheminassab, Arian Saffari, George Ban-Weiss, and Constantinos Sioutas. Emission rates of particle number, mass and black carbon by the los angeles international airport (lax) and its impact on air quality in los angeles. *Atmospheric Environment*, 151:82–93, 2017.

[18] N Hudda, MC Simon, W Zamore, and JL Durant. Aviation-related impacts on ultrafine particle number concentrations outside and inside residences near an airport. *Environmental science & technology*, 52(4):1765–1772, 2018.

[19] Jörg Sintermann, Urs Schaufelberger, Roy Eugster, and Michael Götsch. Ultrafeine partikel in kloten 2019 & 2020, belastungssituation und einfluss des flugverkehrs. Technical report, OSTLUFT, 2021.

[20] J. Rissman, S. Arunachalam, M. Woody, J. J. West, T. BenDor, and F. S. Binkowski. A plume-in-grid approach to characterize air quality impacts of aircraft emissions at the hartsfield–jackson atlanta international airport. *Atmospheric Chemistry and Physics*, 13(18):9285–9302, 2013.

[21] M.C. Woody, H.-W. Wong, J.J. West, and S. Arunachalam. Multiscale predictions of aviation-attributable pm2.5 for u.s. airports modeled using cmaq with plume-in-grid and an aircraft-specific 1-d emission model. *Atmospheric Environment*, 147:384–394, 2016.

[22] LP Vennam, W Vizuete, K Talgo, M Omary, FS Binkowski, J Xing, R Mathur, and

S Arunachalam. Modeled full-flight aircraft emissions impacts on air quality and their sensitivity to grid resolution. *Journal of Geophysical Research: Atmospheres*, 122(24):13–472, 2017.

[23] Xiaole Zhang, Matthias Karl, Luchi Zhang, and Jing Wang. Influence of aviation emission on the particle number concentration near zurich airport. *Environmental Science & Technology*, 54(22):14161–14171, 2020.

[24] R.A Almbauer, D Oettl, M Bacher, and P.J Sturm. Simulation of the air quality during a field study for the city of graz. *Atmospheric Environment*, 34(27):4581–4594, 2000.

[25] Dietmar Oettl, Peter Johann Sturm, Michael Bacher, Gerhard Pretterhofer, and Raimund Alfons Almbauer. A simple model for the dispersion of pollutants from a road tunnel portal. *Atmospheric Environment*, 36(18):2943–2953, 2002.

[26] A. Berchet, K. Zink, D. Oettl, J. Brunner, L. Emmenegger, and D. Brunner. Evaluation of high-resolution gramm–gral (v15.12/v14.8) no_x simulations over the city of zürich, switzerland. *Geoscientific Model Development*, 10(9):3441–3459, 2017.

[27] Matthias Karl, Allan Gross, Liisa Pirjola, and Caroline Leck. A new flexible multicomponent model for the study of aerosol dynamics in the marine boundary layer. *Tellus B: Chemical and Physical Meteorology*, 63(5):1001–1025, 2011.

[28] Matthias Schäfer, Martin Strohmeier, Vincent Lenders, Ivan Martinovic, and Matthias Wilhelm. Bringing up opensky: A large-scale ads-b sensor network for research. In *IPSN-14 Proceedings of the 13th International Symposium on Information Processing in Sensor Networks*, pages 83–94, 2014.

[29] Flughafen-Zürich. *Statistic Report 2019*. Flughafen Zürich AG, 2020.

[30] Flughafen-Zürich. *Statistic Report 2020*. Flughafen Zürich AG, 2021.

[31] European-Environment-Agency. Emep/eea air pollutant emission inventory guidebook 2019: technical guidance to prepare national emission inventories. *EEA-Report*, 2019.

[32] Xiaowen Yang, Shuiyuan Cheng, Jianlei Lang, Ran Xu, and Zhe Lv. Characterization of aircraft emissions and air quality impacts of an international airport. *Journal of Environmental Sciences*, 72:198–207, 2018.

[33] Richard H Moore, Michael Shook, Andreas Beyersdorf, Chelsea Corr, Scott Herndon, W Berk Knighton, Richard Miake-Lye, K Lee Thornhill, Edward L Winstead, Zhenhong Yu, et al. Influence of jet fuel composition on aircraft engine emissions: A

synthesis of aerosol emissions data from the nasa apex, aafex, and access missions. *Energy & Fuels*, 29(4):2591–2600, 2015.

[34] Richard H Moore, Michael A Shook, Luke D Ziemba, Joshua P DiGangi, Edward L Winstead, Bastian Rauch, Tina Jurkat, Kenneth L Thornhill, Ewan C Crosbie, Claire Robinson, et al. Take-off engine particle emission indices for in-service aircraft at los angeles international airport. *Scientific data*, 4(1):1–15, 2017.

[35] Hsi-Wu Wong, Mina Jun, Jay Peck, Ian A Waitz, and Richard C Miake-Lye. Roles of organic emissions in the formation of near field aircraft-emitted volatile particulate matter: A kinetic microphysical modeling study. *Journal of Engineering for Gas Turbines and Power*, 137(7):072606, 2015.

[36] Benjamin T Brem, Lukas Durdina, Frithjof Siegerist, Peter Beyerle, Kevin Bruderer, Theo Rindlisbacher, Sara Rocci-Denis, M Gurhan Andac, Joseph Zelina, Olivier Penanhoat, et al. Effects of fuel aromatic content on nonvolatile particulate emissions of an in-production aircraft gas turbine. *Environmental science & technology*, 49(22):13149–13157, 2015.

[37] Lukas Durdina, Benjamin T Brem, Ari Setyan, Frithjof Siegerist, Theo Rindlisbacher, and Jing Wang. Assessment of particle pollution from jetliners: from smoke visibility to nanoparticle counting. *Environmental Science & Technology*, 51(6):3534–3541, 2017.

[38] Morten Winther, Uffe Kousgaard, Thomas Ellermann, Andreas Massling, Jacob Klenø Nøjgaard, and Matthias Ketzel. Emissions of nox, particle mass and particle numbers from aircraft main engines, apu's and handling equipment at copenhagen airport. *Atmospheric Environment*, 100:218–229, 2015.

[39] Dietmar Oettl. Documentation of the prognostic mesoscale model gramm (graz mesoscale model) version 20.09. Technical report, Graz University of Technology, 2020.

[40] Dietmar Oettl. Documentation of the lagrangian particle model gral (graz lagrangian model) version 21.09. Technical report, Graz University of Technology, 2021.

[41] Desmond T Bailey. *Meteorological monitoring guidance for regulatory modeling applications*. DIANE Publishing, 2000.

[42] Dietmar Oettl. Recommendations when using the gral/gramm modelling system, version 20.03. Technical report, Graz University of Technology, 2020.

[43] Tom G Farr, Paul A Rosen, Edward Caro, Robert Crippen, Riley Duren, Scott Hensley, Michael Kobrick, Mimi Paller, Ernesto Rodriguez, Ladislav Roth, et al. The shuttle radar topography mission. *Reviews of geophysics*, 45(2), 2007.

[44] C Steinmeier. Corine land cover 2000/2006 switzerland. final report, 2017.

[45] M. Karl, J. Kukkonen, M. P. Keuken, S. Lützenkirchen, L. Pirjola, and T. Hussein. Modeling and measurements of urban aerosol processes
on the neighborhood scale in rotterdam,
oslo and helsinki. *Atmospheric Chemistry and Physics*, 16(8):4817–4835, 2016.

[46] L. Pirjola, M. Karl, T. Rönkkö, and F. Arnold. Model studies of volatile diesel exhaust particle formation: are organic vapours involved in nucleation and growth? *Atmospheric Chemistry and Physics*, 15(18):10435–10452, 2015.

[47] Matthias Karl, Caroline Leck, Esther Coz, and Jost Heintzenberg. Marine nanogels as a source of atmospheric nanoparticles in the high arctic. *Geophysical research letters*, 40(14):3738–3743, 2013.

[48] Matthias Karl. Multicomponent aerosol formation model mafor model version 1.9.9 user's guide. Technical report, Chemistry Transport Modelling, Helmholtz-Zentrum Hereon, 2021.

[49] N. Bukowiecki, J. Dommen, A. S. H. Prévôt, E. Weingartner, and U. Baltensperger. Fine and ultrafine particles in the zürich (switzerland) area measured with a mobile laboratory: an assessment of the seasonal and regional variation throughout a year. *Atmospheric Chemistry and Physics*, 3(5):1477–1494, 2003.

[50] Nicholas Metropolis and Stanislaw Ulam. The monte carlo method. *Journal of the American statistical association*, 44(247):335–341, 1949.

[51] E Fleuti and S Maraini. Taxi-emissions at zurich airport-calculation analysis and opportunities. *Flughafen Zürich AG*, 2017.

[52] Selina Wolfisberg, Claudia Gregoriano, Tristan Struja, Alexander Kutz, Daniel Koch, Luca Bernasconi, Angelika Hammerer-Lercher, Christine Mohr, Sebastian Haubitz, Anna Conen, et al. Comparison of characteristics, predictors and outcomes between the first and second covid-19 waves in a tertiary care centre in switzerland: an observational analysis. *Swiss medical weekly*, 151(3132), 2021.

[53] David Hasenfratz, Olga Saukh, Christoph Walser, Christoph Hueglin, Martin Fierz, Tabita Arn, Jan Beutel, and Lothar Thiele. Deriving high-resolution urban air pollution maps using mobile sensor nodes. *Pervasive and Mobile Computing*, 16:268–285, 2015. Selected Papers from the Twelfth Annual IEEE International Conference on Pervasive Computing and Communications (PerCom 2014).

[54] LAWA. Statistics - 10-year summary - faa aircraft movements.

Appendices

A1 Aircraft Statistics

Table A1: Statistics of flight movements by aircraft types in Zurich airport 2019.

Company	Aircraft type	Number of flight
Airbus	A300	6
	A310	106
	A318	1,584
	A319	26,429
	A320	72,004
	A321	22,242
	A330	12,881
	A340	4,626
	A350	1,981
	A380	2,161
Antonov	AN12/22/26/72/124	8
ATR	AT43/45	2
	AT72/76	127
Beechcraft	1900	776
Boeing	B737	8,813
	B747	100
	B757	615
	B767	2,115
	B777	6,724
	B787	2,182
Bombardier	Cseries	33,660
	Dash 8	4,043
	Canadair	3,460
British Aerospace	Avro Jet	46
Dornier(Fairchild)	D328/J328	8
Embraer	E135/145	14
	E170/175	2,155
	E190/195	31,100
Fokker	F100	989
Douglas	MD80/MD90	42
SAAB	2000/SF340	2,106
Others	-	7
Total	-	243,112

Table A2: Statistics of flight movements by aircraft types in Zurich airport 2020.

Company	Aircraft	Number of flight
Airbus	A220	15171
	A300	76
	A318	374
	A319	7,488
	A320	22,744
	A321	6,555
	A330	3,251
	A340	2,142
	A350	1,144
	A380	492
Antonov	AN12/22/26/72/124	6
ATR	AT43/45/72/75/76	14
Beechcraft	200/1900	168
Boeing	B737	3,710
	B747	38
	B757	111
	B767	481
	B777	4,439
	B787	1,607
Bombardier	Dash 8	1,165
	Canadair	1,550
British Aerospace	Avro Jet	3
Dornier (Fairchild)	D328	2
Embraer	E170/175	803
	E190/195	9,453
Fokker	F50/F100	71
McDonnell Douglas	MD80/MD90	4
SAAB	2000/SF340	14
Others	-	5
Total	-	83,081

A2 Annual spatial distribution of PN emission

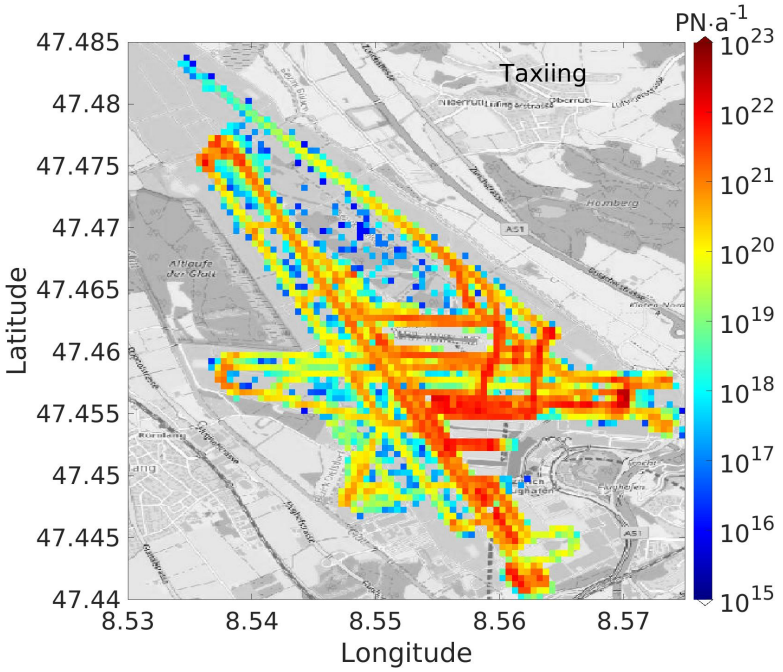

Figure A1: Spatial distribution of the particle number emissions during the taxi phase in the year of 2019. The reference coordinate system shown on the x and y-axis is WGS 84 (EPSG:4326).

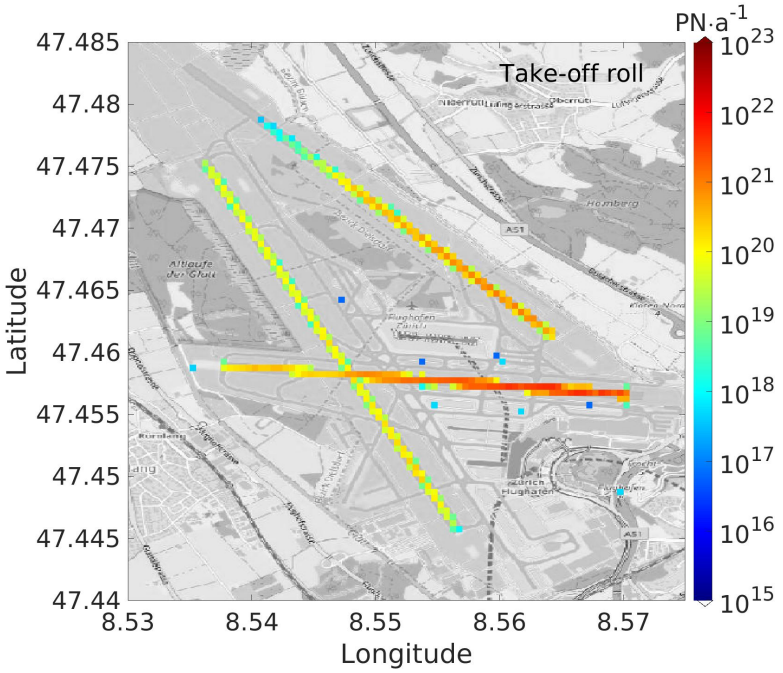

Figure A2: Spatial distribution of the particle number emissions during the take-off/roll phase in the year of 2019. The reference coordinate system shown on the x and y-axis is WGS 84 (EPSG:4326).

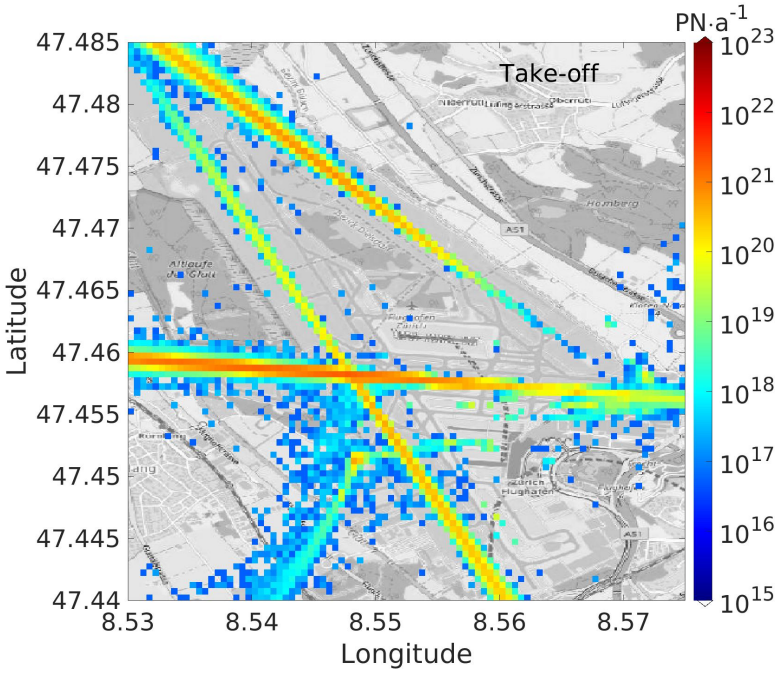

Figure A3: Spatial distribution of the particle number emissions during the take-off phase in the year of 2019. The reference coordinate system shown on the x and y-axis is WGS 84 (EPSG:4326).

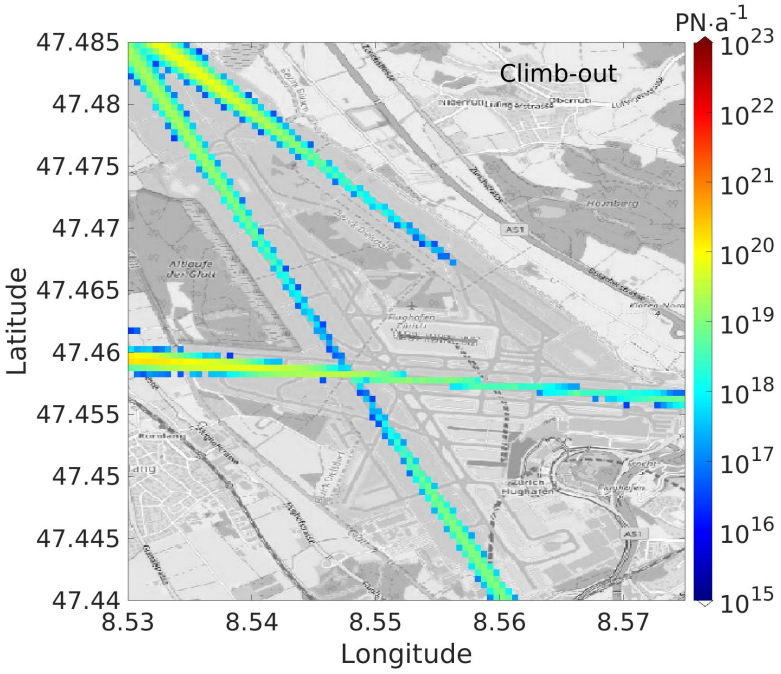

Figure A4: Spatial distribution of the particle number emissions during the climb-out phase in the year of 2019. The reference coordinate system shown on the x and y-axis is WGS 84 (EPSG:4326).

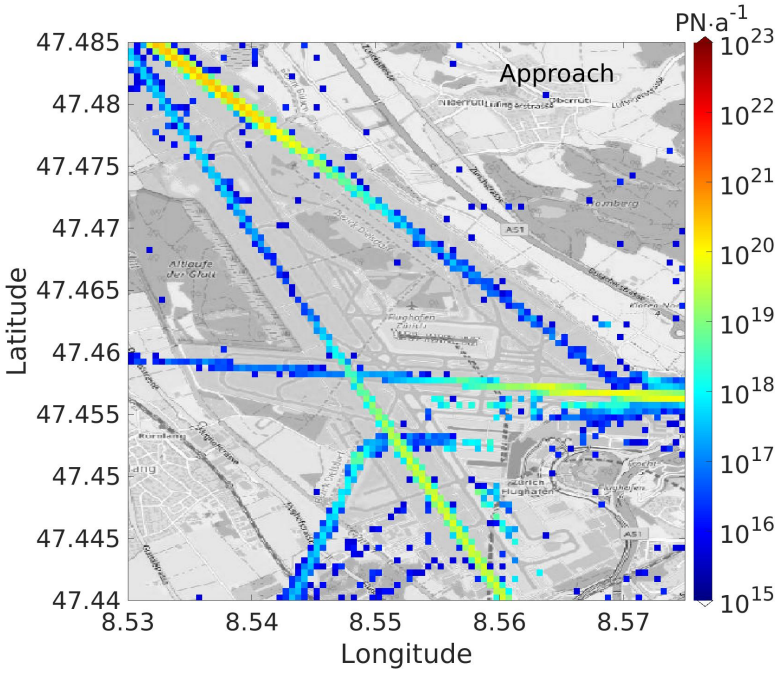

Figure A5: Spatial distribution of the particle number emissions during the approach phase in the year of 2019. The reference coordinate system shown on the x and y-axis is WGS 84 (EPSG:4326).

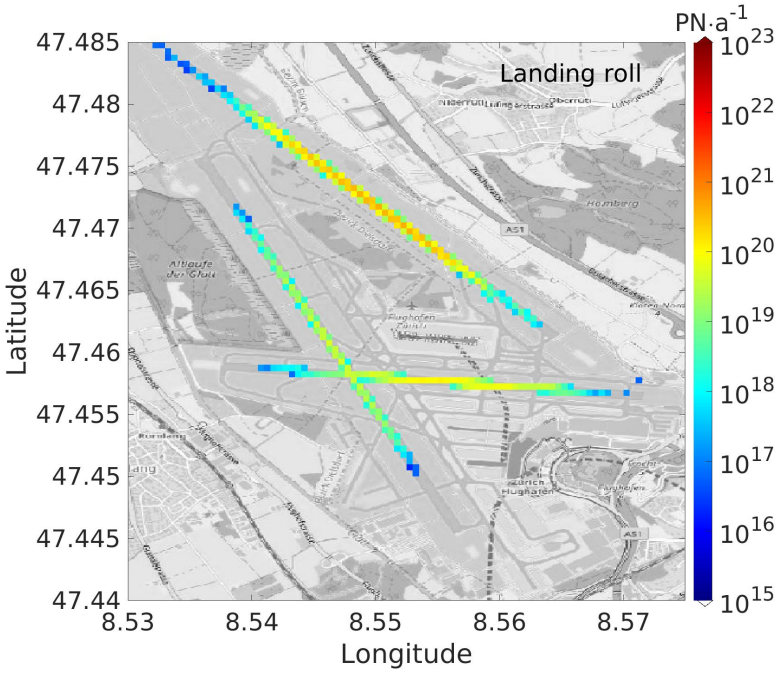

Figure A6: Spatial distribution of the particle number emissions during the landing phase in the year of 2020. The reference coordinate system shown on the x and y-axis is WGS 84 (EPSG:4326).

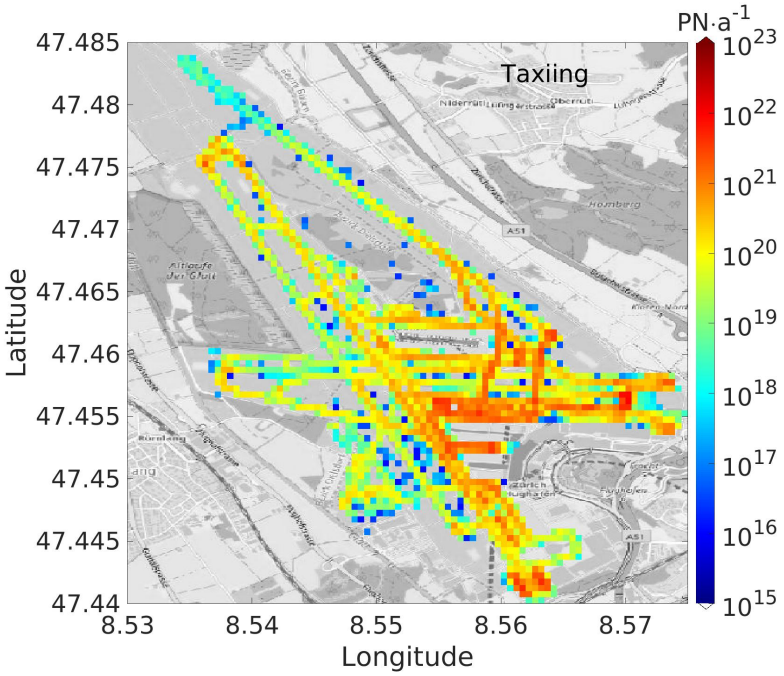

Figure A7: Spatial distribution of the particle number emissions during the taxi phase in the year of 2020. The reference coordinate system shown on the x and y-axis is WGS 84 (EPSG:4326).

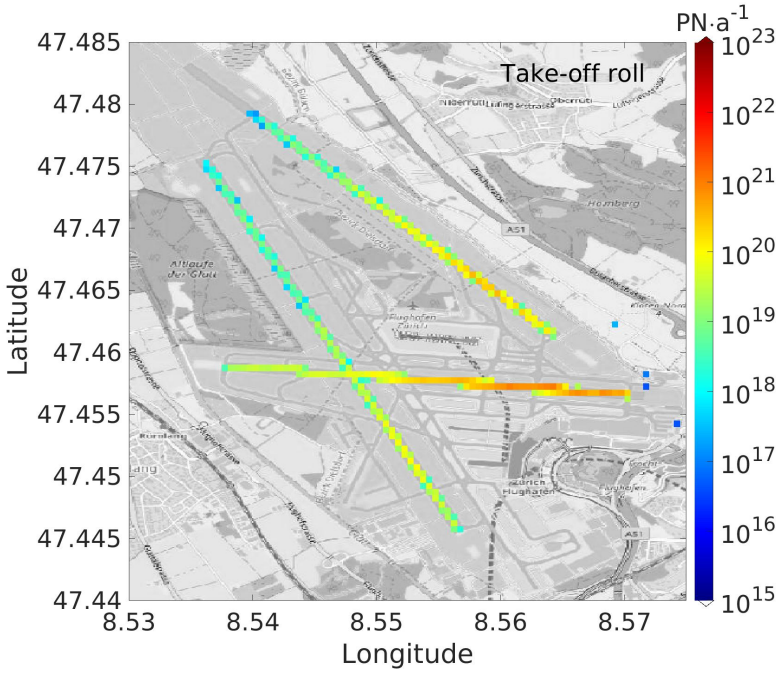

Figure A8: Spatial distribution of the particle number emissions during the take-off/roll phase in the year of 2020. The reference coordinate system shown on the x and y-axis is WGS 84 (EPSG:4326).

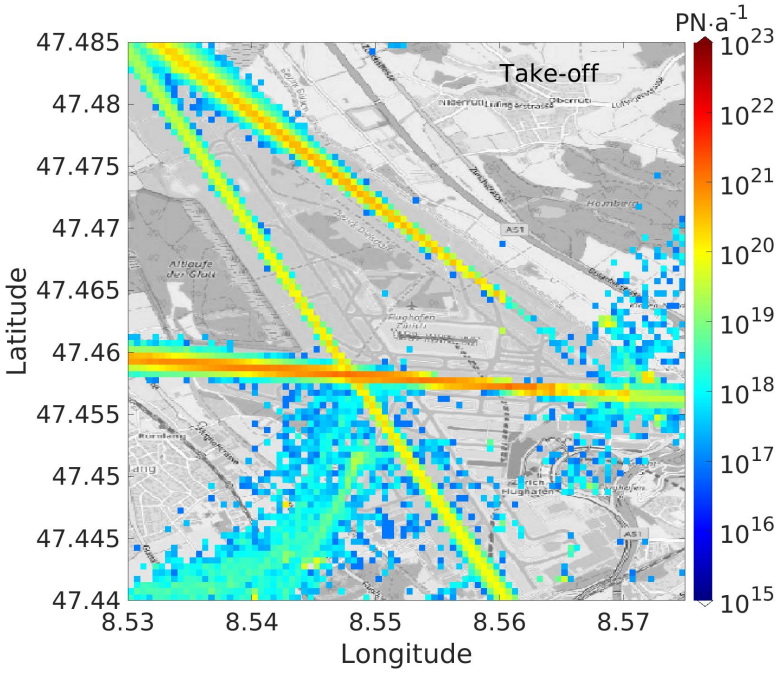

Figure A9: Spatial distribution of the particle number emissions during the take-off phase in the year of 2020. The reference coordinate system shown on the x and y-axis is WGS 84 (EPSG:4326).

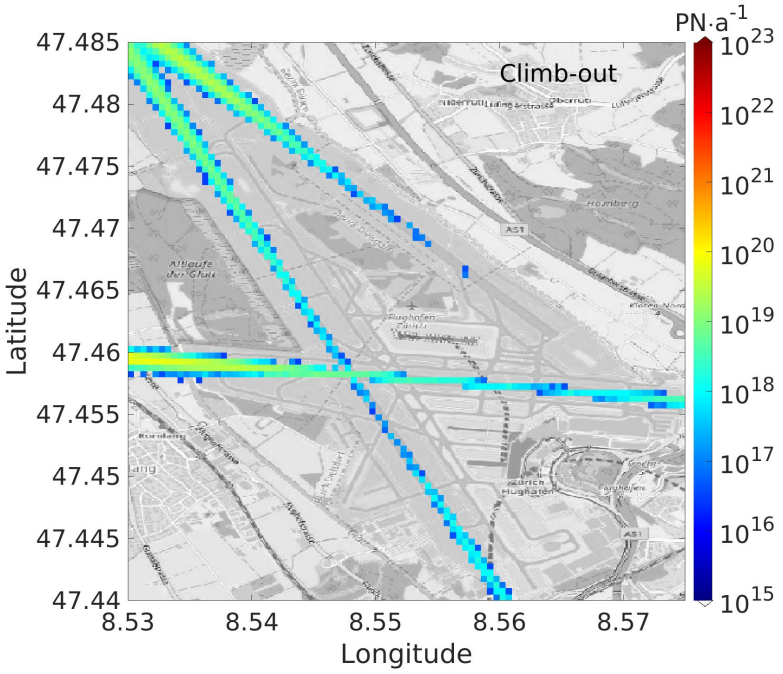

Figure A10: Spatial distribution of the particle number emissions during the climb-out phase in the year of 2020. The reference coordinate system shown on the x and y-axis is WGS 84 (EPSG:4326).

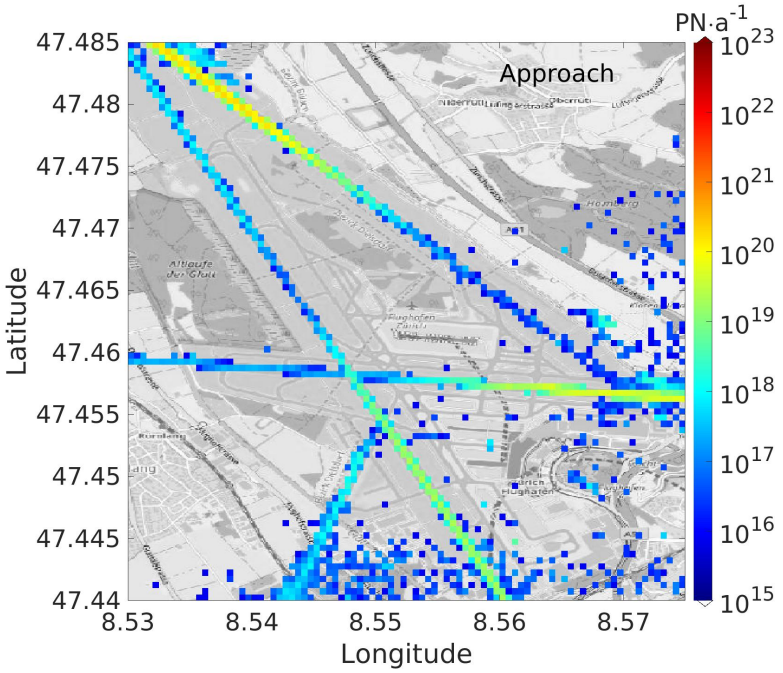

Figure A11: Spatial distribution of the particle number emissions during the approach phase in the year of 2020. The reference coordinate system shown on the x and y-axis is WGS 84 (EPSG:4326).

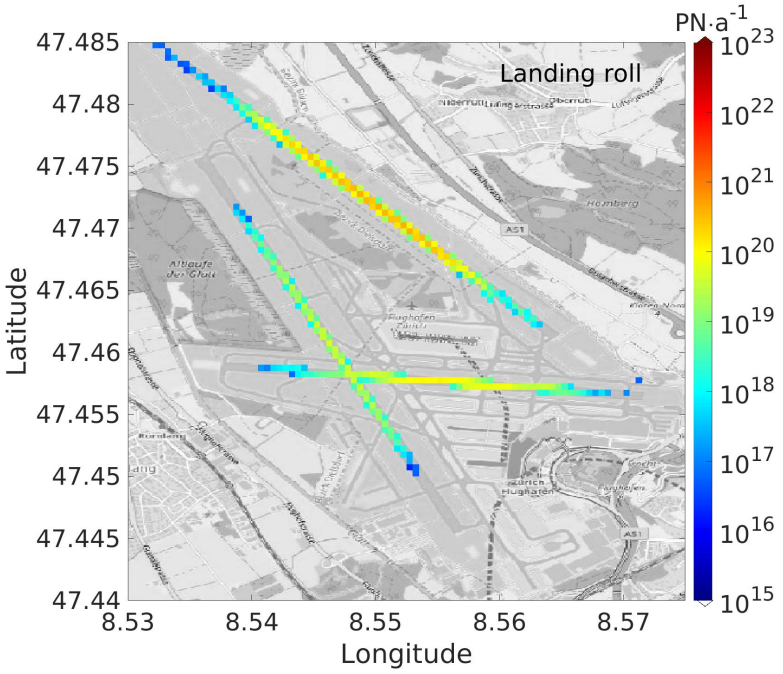

Figure A12: Spatial distribution of the particle number emissions during the landing phase in the year of 2020. The reference coordinate system shown on the x and y-axis is WGS 84 (EPSG:4326).

A3 PN emission influence to the simulated PN concentration

Table A3: Share [%] of PN emission from each flight phase which quantified how much it influenced the predicted PN concentration at the monitoring station in Kloten.

Year	Taxi	Take-off roll	Take-off	Climb-out	Approach	Landing
2019	88.53	8.58	1.07	0.06	0.37	1.40
2020	90.28	4.74	3.12	0.03	0.80	1.03

A4 Estimation of the background concentration

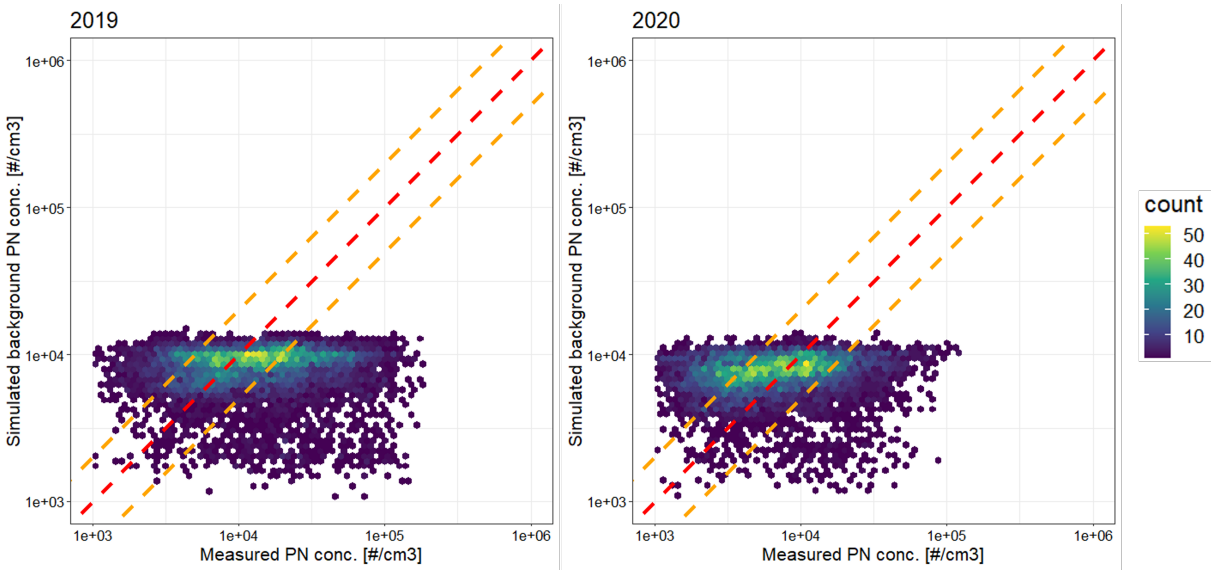

Figure A13: Scatter plots of estimated background PN concentrations from the SVM model versus the measured hourly PN concentrations from the monitoring station in 2019 and 2020. A heat map was presented to illustrate the distribution of scatter points in the plots.